ITCZ Breakdown and Its Upscale Impact on the Planetary-Scale Circulation over the Eastern Pacific

Qiu Yang* and Andrew J. Majda

Department of Mathematics and Center for Atmosphere Ocean Science, Courant Institute of Mathematical Sciences, New York University, New York, NY, USA

Boualem Khouider

Department of Mathematics and Statistics, University of Victoria, Victoria, BC, Canada

**Corresponding author address:* Qiu Yang, Courant Institute of Mathematical Sciences, New York University, 251 Mercer Street, New York, NY, 10012

E-mail: yangq@cims.nyu.edu

ABSTRACT

The Intertropical Convergence Zone (ITCZ) over the eastern Pacific is sometimes observed to break down into several vortices on the synoptic time scale. It is still a challenge for present-day numerical models to simulate the ITCZ breakdown in the baroclinic modes. Also, the upscale impact of the associated mesoscale fluctuations on the planetary-scale circulation is not well understood. Here a simplified multi-scale model for the modulation of the ITCZ is used to study these issues. A prescribed two-scale heating drives the planetary-scale circulation through both planetary-scale mean heating and eddy flux divergence of zonal momentum, where the latter represents the upscale impact of mesoscale fluctuations. In an idealized scenario with zonally symmetric planetary-scale flow, both deep convective heating and shallow congestus heating are considered. First, several key features of the ITCZ breakdown in the baroclinic modes are captured in this multi-scale model. Secondly, the eddy flux divergence of zonal momentum is characterized by mid-level (low-level) eastward (westward) momentum forcing at high latitudes of the Northern Hemisphere and alternate mid-level momentum forcing at low latitudes. Such upscale impact of mesoscale fluctuations tends to accelerate (decelerate) planetary-scale zonal jets in the middle (lower) troposphere. Thirdly, compared with deep convective heating, shallow congestus heating induces stronger vorticity anomalies on the mesoscale and more significant eddy flux divergence of zonal momentum and acceleration/deceleration effects on the planetary-scale mean flow. In a more realistic scenario with zonally varying planetary-scale flow, the most significant zonal velocity anomalies are confined in the diabatic heating region.

1. Introduction

The ITCZ is a narrow band of cloudiness encircling the Earth in the tropics. Due to the low heat capacity of the continental regions, a large portion of energy that originally comes from insolation is released back to the troposphere in the form of longwave radiation, providing favorable conditions for tropical convection in the ITCZ (Ramage 1968). Over the oceanic regions, convective activity in the ITCZ is accompanied by warm sea surface temperatures, which increases evaporation and heat influx through the atmospheric boundary layer (Zhang 2001). Besides, low pressure in the ITCZ induces wind convergence in the lower troposphere with the northeasterly trade winds to its north and southeasterly trade winds to its south (Toma and Webster 2010a). The early observational studies based on satellite imagery can date back to the 1960s, where the variation of the visible brightness field affected by all cloud types is used to estimate the convective field with cloudiness (Hanson et al. 1967; Hubert et al. 1969; Winston 1971; Gruber 1972). With the development of satellite measurement in higher spatiotemporal resolutions, global-scale analysis for the ITCZ has been done based on long-record satellite datasets, providing the community with concise descriptions of global ITCZ climatology (Waliser and Gautier 1993). In general, the ITCZ in the continental regions such as Africa and South America and most of the oceanic regions such as the Indian Ocean, the western Pacific and Atlantic Ocean migrates between the Northern and Southern Hemispheres with the seasonal cycle. However, the eastern Pacific ITCZ remains in the Northern Hemisphere along the latitudes between $5°N$ and $15°N$ all year round. Such persistent location of the eastern Pacific ITCZ in the Northern Hemisphere has attracted attention of the community, and many theoretical and numerical studies have been undertaken to illustrate the underlying mechanism (Philander et al. 1996). Climate models fail to capture this Northern

Hemisphere persistence of the ITCZ, which is associated with the so-called double ITCZ problem (Hubert et al. 1969; Zhang 2001; Lin 2007).

Instead of being a steady state, the ITCZ over the eastern Pacific is sometimes observed to undulate and break down on the synoptic time scale (Ferreira and Schubert 1997). In details, the ITCZ first undulates and breaks down into several disturbances in the form of displaced cloud clusters at different locations. Among these disturbances, some grow to become tropical cyclones and others dissipate in the following several days. As tropical cyclones move to high latitudes, a new ITCZ band of cloudiness reforms in the original place. This whole process is referred to the ITCZ breakdown. Since most of tropical cyclones forming near the ITCZ (Gray 1979) can significantly impact the local weather and global atmospheric conditions, many physical mechanisms have been proposed to explain the ITCZ breakdown. For instance, easterly waves are frequently observed in the Atlantic Ocean, West Africa and the Pacific (Toma and Webster 2010a,b), which can be an external reason for the ITCZ breakdown as the westward moving synoptic-scale disturbances propagate to the eastern Pacific and disturb the ITCZ flow field (Gu and Zhang 2002). In addition, internal instability such as the vortex roll-up mechanism (Hack et al. 1989; Ferreira and Schubert 1997) involving a reversed meridional potential vorticity gradient field is proposed to explain the ITCZ breakdown. As the ITCZ undulates and breaks down into disturbances, the atmospheric flows get disturbed with cyclonic flows, which further impact the large-scale circulation over the eastern Pacific (Wang and Magnusdottir 2006).

In spite of many observational studies based on satellite measurement, understanding the essential mechanism for the ITCZ breakdown and its upscale impact on the planetary-scale circulation is still an unsolved problem. For example, the barotropic aspects of the ITCZ breakdown are examined through a nonlinear shallow water model on the sphere (Ferreira and Schubert 1997). After prescribing a zonally elongated mass sink near the equator, a potential vorticity strip with a reversed meridional gradient appears on the poleward side of the mass sink, which is unstable with weak disturbances and resembles the ITCZ breakdown. However, since the eastern Pacific ITCZ is characterized as a narrow band of cloudiness, convective activity increases the buoyancy of air parcels and lift them into the upper troposphere. Such baroclinic aspects of the ITCZ breakdown are not captured by the shallow water model in (Ferreira and Schubert 1997). On the other hand, three-dimensional simulations using a primitive equation model have been used to model the atmospheric flows during the ITCZ breakdown (Wang and Magnusdottir 2005). In that work, a positive potential vorticity strip is generated in the lower troposphere of the Northern Hemisphere with a reversed meridional gradient, while the potential vorticity in the upper troposphere is negative with a broader meridional extent. As the potential vorticity strip undulates and breaks down, the resulting vorticity anomalies resemble the tropical cyclones over several hundred kilometers in the eastern Pacific ITCZ. However, the upscale impact of the atmospheric flows associated with the ITCZ breakdown on the planetary-scale circulation is still unclear (Wang and Magnusdottir 2005). The goal of this paper is to use a simple multi-scale model to address those issues including the baroclinic aspects of the ITCZ breakdown and the upscale impact of mesoscale fluctuations on the planetary-scale circulation through eddy flux divergence of zonal momentum.

Tropical convection is organized in a hierarchical structure across multiple spatiotemporal scales, ranging from the single cumulus cloud over several kilometers, to mesoscale convective systems (Houze 2004), to synoptic-scale convectively coupled equatorial waves (Kiladis et al. 2009) to planetary-scale intraseasonal oscillations such as the Madden-Julian Oscillation (Zhang 2005). In the theoretical directions, self-consistent multi-scale models based on multi-scale asymptotic methods were derived systematically and used to describe such hierarchical structures of atmospheric flows in the tropics (Majda and Klein 2003; Majda 2007). The advantages of using these multi-scale models lie in isolating the essential components of multi-scale interaction and providing assessment of the upscale impact of the small-scale fluctuations onto the large-scale mean flow through eddy flux divergence of momentum and temperature in a transparent fashion. In particular, the modulation of the ITCZ (M-ITCZ) equations (Biello and Majda 2013) describe atmospheric flows on both the mesoscale and planetary scale, which interact with each other in a completely nonlinear way. Such complete nonlinearity distinguishes itself from other multi-scale models (Biello and Majda 2005, 2006; Majda 2007; Biello et al. 2010; Majda et al. 2010; Yang and Majda 2014; Majda and Yang 2016), where large-scale mean flow and small-scale fluctuations are typically governed by different groups of equations. Here a specific numerical scheme is designed to achieve satisfactory accuracy without violating the asymptotic assumptions after the discretization of the multi-scale system.

The M-ITCZ equations describe atmospheric dynamics on both the mesoscale and planetary scale, which are the typical scales of atmospheric flows in the eastern Pacific ITCZ. On the one hand, a single tropical cyclone and the associated cyclonic flows during the ITCZ breakdown have a comparable size as the mesoscale components in the M-ITCZ equations, and they are driven by latent heat release during precipitation of cloud clusters. On the other hand, the planetary-scale velocity and temperature fields in the M-ITCZ equations can be used to mimic the large-scale circulation pattern over the eastern Pacific, which is characterized by a strong overturning circulation cell around the equator. Here the M-ITCZ equations are used to simulate the ITCZ breakdown and its upscale impact of the disturbed atmospheric flows associated with tropical cyclones on the planetary-scale circulation. To begin with, an idealized scenario with zonal symmetry on the planetary scale is considered so that the planetary-scale gravity wave is suppressed. On the mesoscale, zonally localized heating is prescribed in the Northern Hemisphere to mimic diabatic heating associated with a single cloud cluster in the eastern Pacific ITCZ. Outside this heating region, horizontally uniform cooling is prescribed to mimic radiative cooling and subsiding motion in the cold and dry region such as the whole Southern Hemisphere (Toma and Webster 2010a). Besides deep meridional circulation in the eastern Pacific ITCZ, shallow meridional circulation with northerly returning flows just above the atmospheric boundary layer is observed by satellite measurement and dropsondes and wind profilers (Zhang et al. 2004; Nolan et al. 2007; Zhang et al. 2008). Since the large-scale meridional circulation can be regarded as a response to convective heating (Schneider and Lindzen 1977; Gill 1980; Wu 2003), the resulting mesoscale solutions in the M-ITCZ equations driven by deep convective heating and shallow congestus heating are compared in terms of their different upscale impact. In fact, the deep and shallow ITCZ breakdown classified by convection depth have been observed and studied in (Wang and Magnusdottir 2006). Then a more realistic scenario including both mesoscale and planetary-scale dynamics is considered with the diabatic heating modulated by a convective envelope to mimic the eastern Pacific ITCZ. The upscale impact of mesoscale fluctuations during the ITCZ breakdown can induce rectification of the planetary-scale circulation over the eastern Pacific.

After prescribing the diabatic heating for latent heat release in the eastern Pacific ITCZ, the M-ITCZ equations are initialized from a background state of rest and numerically integrated when forced by the diabatic heating. Several crucial results are obtained by diagnostically calculating eddy flux divergence of zonal momentum and comparing the flow fields with mesoscale zonally localized and uniform heating in the first scenario. First, a positive vorticity strip is generated in the northern side of the deep diabatic heating region in the lower troposphere and undulates in the first two days, followed by the formation of a strong vortex in the middle, which resembles the ITCZ breakdown as seen in observations (Ferreira and Schubert 1997). In the middle troposphere, a pair of vorticity dipoles form at low latitudes of the Northern Hemisphere. The baroclinic aspects of the ITCZ breakdown is examined here, including the vertical structure of vorticity and flow fields. Secondly, in the deep heating case, the eddy flux divergence of zonal momentum is characterized by mid-level (low-level) eastward (westward) momentum forcing at high latitudes of the Northern Hemisphere and alternate mid-level momentum forcing at low latitudes. As far as kinetic energy is concerned, such eddy impact of the mesoscale dynamics accelerate mid-level zonal jets at both low and high latitudes, and decelerate low-level zonal jets at high latitudes. Thirdly, compared with deep convective heating, shallow congestus heating efficiently drives stronger vorticity anomalies and induces more significant eddy flux divergence of zonal momentum and acceleration/deceleration effects in the Northern Hemisphere, although the flow fields are confined in the shallower levels. In the more realistic scenario where the mesoscale fluctuations are coupled to the planetary-scale gravity waves, it is found that the most significant zonal velocity anomalies are confined to the diabatic heating region while small zonal velocity anomalies are transported away by the planetary-scale gravity waves. As for the rectification of the planetary-scale circulation in the Northern Hemisphere, westerly wind anomalies are induced at high latitudes of the lower and middle troposphere and low latitudes of the upper troposphere, while easterly wind anomalies are induced around the equator in the middle troposphere.

The rest of this paper is organized as follows. The properties of the M-ITCZ equations for mesoscale barotropic Rossby waves and planetary-scale gravity waves and conservation of potential vorticity and kinetic energy are discussed in Sec.2. Sec.3 presents numerical solutions for the ITCZ breakdown in zonally symmetric planetary-scale flow. Both deep convective heating and shallow congestus heating cases are considered in the same model setup and compared in terms of vorticity field, eddy flux divergence of zonal momentum and acceleration/deceleration effects on the mean flow. Sec.4 considers the general case where the diabatic heating is modulated by a planetary-scale convective envelope, explaining the rectification of the planetary-scale circulation due to the ITCZ breakdown over the eastern Pacific. The paper ends with a concluding discussion. The numerical scheme for solving the M-ITCZ equations is summarized in the Appendix.

2. Properties of the M-ITCZ Equations

a. The governing equations

Inspired by the multi-scale features of tropical convection, the multi-scale asymptotic methods were used to derive reduced models across multiple spatiotemporal scales (Majda and Klein 2003; Majda 2007). In particular, the M-ITCZ equations, derived in (Biello and Majda 2013), describes the multi-scale dynamics of the ITCZ from the diurnal to monthly time scales in which mesoscale convectively coupled Rossby waves are modulated by large-scale gravity waves. The M-ITCZ equations in dimensionless units read as follows,

$$\frac{Du}{Dt} - yv = -\frac{\partial p}{\partial x} - \frac{\partial \Pi}{\partial X} - du, \tag{1a}$$

$$\frac{Dv}{Dt} + yu = -\frac{\partial p}{\partial y} - dv, \tag{1b}$$

$$w = S^{\theta}, \tag{1c}$$

$$\frac{\partial u}{\partial x} + \frac{\partial v}{\partial y} + \frac{\partial w}{\partial z} = 0, \tag{1d}$$

$$\frac{\partial \Pi}{\partial x} = \frac{\partial \Pi}{\partial y} = 0, \ \frac{\partial \Pi}{\partial z} = \Theta, \tag{1e}$$

$$\frac{\partial \Theta}{\partial t} + \langle \bar{w} \rangle \frac{\partial \Theta}{\partial z} + W = 0, \tag{1f}$$

$$\frac{\partial}{\partial X}\left[\langle \bar{u} \rangle - U\right] + \frac{\partial W}{\partial z} = 0, \tag{1g}$$

where $\frac{D}{Dt} = \frac{\partial}{\partial t} + u\frac{\partial}{\partial x} + v\frac{\partial}{\partial y} + w\frac{\partial}{\partial z}$ is the advection derivative due to the three-dimensional flow.

The M-ITCZ equations are derived by using multi-scale asymptotic methods and introducing two zonal spatial scales (planetary-scale X, mesoscale x). More details about the derivation can be found in (Biello and Majda 2013). In Eqs.1a-1g, one dimensionless unit of planetary-scale X and mesoscale x correspond to $L_p = 5000km$ and $L_m = 500km$, respectively, and that of time t is 1 *day*. The Rossby number, $\varepsilon = 0.1$, is the small nondimensional parameter used in the asymptotic analysis. The M-ITCZ equations involve velocity field (u, v, w) and pressure perturbation p balancing the equations of motion at $\mathscr{O}(1)$, large-scale pressure Π and large-scale potential temperature Θ at $\mathscr{O}\left(\varepsilon^{-1}\right)$ as well as secondary vertical flow W at $\mathscr{O}(\varepsilon)$. The velocity field (u, v, w) and pressure perturbation p depend on both zonal spatial scales (planetary-scale X, mesoscale x) as well as the meridional coordinate y while the large-scale pressure Π and potential temperature Θ only depend on the planetary-scale zonal coordinate X. All physical variables can have vertical dependence z and temporal variation t. One dimensionless unit of horizontal velocity (u, v) corresponds to 5 ms^{-1} , one dimensionless unit of vertical velocity w corresponds to 0.05 ms^{-1} and that of pressure perturbation, per unit mass, is 25 m^2s^{-2}. The large-scale pressure Π and temperature perturbation Θ are in units of 250 m^2s^{-2} and 3.3 K, respectively. The secondary vertical flow W has units of 0.005 ms^{-1}. In this scaling regime, one dimensionless unit of the diabatic heating corresponds to 33 $Kday^{-1}$. Eq.1f-1g involve mesoscale zonal and meridional averaging operators defined for an arbitrary function f as follows.

$$\bar{f}(X, y, z, t) = \lim_{L \to \infty} \frac{1}{2L} \int_{-L}^{L} f(x, X, y, z, t)\, dx, \tag{2}$$

$$\langle f \rangle (x, X, z, t) = \frac{1}{2L_*} \int_{-L_*}^{L_*} f(x, X, y, z, t)\, dy, \tag{3}$$

where L is the mesoscale zonal length of the domain in the asymptotic limit and L_* measures the finite poleward extent of the domain on the equatorial β plane. Besides, U denotes the barotropic mode of mean zonal velocity $\langle \bar{u} \rangle$.

b. Mesoscale barotropic Rossby waves and planetary-scale gravity waves

One crucial feature of the M-ITCZ equations is that the planetary-scale and mesoscale dynamics are nonlinearly coupled with each other. As already mentioned, such a model with complete nonlinearity is quite different from multi-scale models where the flow fields on different scales are governed by different groups of equations. For example, the intraseasonal planetary equatorial synoptic dynamics (IPESD) model consists of two groups of equations (Majda and Biello 2004; Biello and Majda 2005, 2006). One of them describes equatorial synoptic-scale fluctuations and the other one is for the planetary-scale circulations. In the IPESD model, the planetary-scale equations are forced by upscale transfer of momentum and temperature from synoptic-scale fluctuations. In contrast, the M-ITCZ equations consists of only one group of equations, which involve zonal variation on both the planetary scale and mesoscale in a single time scale.

Although both the planetary-scale and mesoscale dynamics in the M-ITCZ equations are completely coupled to each other, the mesoscale dynamics still can be isolated by assuming zonal symmetry of the planetary-scale dynamics. Consequently, the planetary-scale pressure perturbation term $-\Pi_X$ in Eq.1a vanishes, Eqs.1a-1d decouple from Eqs.1e-1g , and the equations for the mesoscale dynamics in dimensionless units become,

$$\frac{Du}{Dt} - yv = -\frac{\partial p}{\partial x} - du, \tag{4a}$$

$$\frac{Dv}{Dt} + yu = -\frac{\partial p}{\partial y} - dv, \tag{4b}$$

$$w = S^{\theta}, \tag{4c}$$

$$\frac{\partial u}{\partial x} + \frac{\partial v}{\partial y} + \frac{\partial w}{\partial z} = 0, \tag{4d}$$

Eqs.4a-4d are called Mesoscale Equatorial Weak Temperature Gradient (MEWTG) equations (Majda and Klein 2003), which consist of three-dimensional velocity field (u, v, w) and pressure perturbation p. The nonlinear horizontal momentum equations on an equatorial β-plane come with a linear momentum damping term, which is used to mimic cumulus drag in large-scale tropical flows (Lin et al. 2005). Due to the Weak Temperature Gradient (WTG) approximation (Sobel et al. 2001), the vertical velocity w is directly determined by the diabatic heating S^{θ}. The conservation of mass is guaranteed by the divergence-free constraint and constant density in the Boussinesq approximation. The MEWTG equations have been applied to model a variety of physical phenomena in the tropical circulation. For example, through a combination of exact solutions and simple numerics, some elementary exact solutions and an exact nonlinear stability analysis about a model similar to the MEWTG equations but on smaller scales and the f-plane are obtained in (Majda et al. 2008). The elementary solutions including the evolution of radial eddies to represent hot towers in a hurricane embryo are studied in a suitable radial preconditioned background. Meanwhile, similar equations to the MEWTG equations also appear in the balanced hot tower model and balanced mesoscale vortex model as dynamical core, which are utilized successfully to illustrate key mechanisms in the hurricane embryo (Majda et al. 2010).

By plugging the ansatz of plane waves into the linear MEWTG equations without thermal forcing and momentum damping, the dispersion relation of barotropic Rossby waves can be obtained (Majda and Klein 2003),

$$\omega = -\frac{k}{k^2 + l^2}, \tag{5}$$

where ω is the frequency and k, l are the wavenumber in the zonal and meridional directions. Such linear solutions with the dispersion relation of barotropic Rossby waves can have arbitrary vertical structure including both barotropic and baroclinic modes, sharing many crucial features of convectively coupled Rossby waves as observed in nature (Kiladis et al. 2009).

As for the planetary-scale dynamics of the M-ITCZ equations, the planetary-scale equations can be obtained by applying the zonal averaging operators defined in Eq.2. In order to guarantee the multi-scale asymptotic assumptions and avoid secular growth, all terms involving mesoscale zonal derivative are assumed to be zero after taking mesoscale zonal averaging. The resulting equations for the planetary-scale gravity wave in dimensionless units read as follows.

$$\frac{\partial \bar{u}}{\partial t}+\frac{\partial}{\partial y}(\bar{v}\bar{u})+\frac{\partial}{\partial z}(\bar{w}\bar{u})-y\bar{v}=-\frac{\partial \Pi}{\partial X}-d\bar{u}-\frac{\partial}{\partial y}\left(\overline{v'u'}\right)-\frac{\partial}{\partial z}\left(\overline{w'u'}\right), \tag{6a}$$

$$\bar{w}=\bar{S}^{\theta}, \tag{6b}$$

$$\frac{\partial \bar{v}}{\partial y}+\frac{\partial \bar{w}}{\partial z}=0, \tag{6c}$$

$$\frac{\partial \Pi}{\partial x}=\frac{\partial \Pi}{\partial y}=0,\ \frac{\partial \Pi}{\partial z}=\Theta, \tag{6d}$$

$$\frac{\partial \Theta}{\partial t}+\langle\bar{w}\rangle\frac{\partial \Theta}{\partial z}+W=0, \tag{6e}$$

$$\frac{\partial}{\partial X}\left[\langle\bar{u}\rangle-U\right]+\frac{\partial W}{\partial z}=0, \tag{6f}$$

where $\langle\bar{w}\rangle$ in Eq.6e vanishes if the rigid boundary condition for meridional velocity $\bar{v}$ is imposed for no inflow and outflow in the meridional boundaries. The prime notation denotes mesoscale zonal fluctuations $f=\bar{f}+f'$, satisfying $\overline{f'}=0$.

Eqs.6a-6f describe zonally propagating gravity waves on the planetary scale. The meridional circulation $(\bar{v},\bar{w})$ is directly determined by the diabatic heating $\overline{S^{\theta}}$ with some suitable boundary conditions. The zonal velocity $\bar{u}$ is forced by advection effects of the meridional circulation$(\bar{v},\bar{w})$, the Coriolis force $y\bar{v}$, planetary-scale zonal gradient of pressure perturbation $-\Pi_X$, momentum damping $-d\bar{u}$ and eddy flux divergence of zonal momentum $-\left(\overline{v'u'}\right)_y-\left(\overline{w'u'}\right)_z$. The meridional mean of zonal velocity in the baroclinic mode and the secondary vertical velocity W have zero divergence. The equations are closed with the hydrostatic balance in Eq.6d and thermal equation in Eq.6e. In fact, the planetary-scale gravity wave equations without upscale fluxes have been studied in (Biello and Majda 2013). By prescribing the diabatic heating in the first baroclinic mode within a zonally localized envelope, planetary-scale gravity waves are generated and propagate in both eastward and westward directions. The planetary-scale gravity waves tend to equalize the meridional mean of the vertical shear of zonal wind at all longitudes in the tropics. Meanwhile, they carry cold temperature anomalies and upward velocity to the west, warm temperature anomalies and downward velocity to the east. In a moist environment, the cold temperature anomalies and upward velocity provide favorable conditions for convection to the west and unfavorable conditions for convection to the east.

c. Conservation of potential vorticity and kinetic energy

Here the conservation of potential vorticity (PV) and kinetic energy in the M-ITCZ equations are discussed.

PV is a useful quantity to understand the generation of vorticity in cyclogenesis, which is materially invariant in flows and can only be changed by diabatic and frictional processes. In the M-ITCZ equations, planetary-scale quantities such as the large-scale pressure perturbation Π_X do not depend on the mesoscale zonal and meridional coordinates (x, y), thus the planetary-scale gravity wave does not directly modify vorticity and PV on the mesoscale except for the advection of the mean zonal velocity. After taking the meridional derivative of Eq.1a and the zonal derivative of Eq.1b along with the thermal equation in Eq.1c and the continuity equation in Eq.1d, the equations for PV can be derived. We have,

$$\frac{DQ}{Dt} = Q\frac{\partial S^\theta}{\partial z} - \frac{\partial v}{\partial z}\frac{\partial S^\theta}{\partial x} + \frac{\partial u}{\partial z}\frac{\partial S^\theta}{\partial y} - d\omega, \tag{7}$$

where $Q = \omega + y$, is the summation of relative vorticity, $\omega = v_x - u_y$, and the vorticity due to earth rotation, y, on an equatorial β-plane.

One simple scenario is that both diabatic heating S^θ and momentum dissipation d are assumed to be zero. Then all terms on the right hand side of Eq.7 vanish and Q is materially invariant. In general, both diabatic heating S^θ and momentum dissipation d are nonzero so that potential vorticity Q is also modified by several terms on the right hand side of Eq.7. The first term $QS^\theta_z =$

Qw_z represents vortex stretching. The second and third terms $-v_z S^\theta_x + u_z S^\theta_y = -v_z w_x + u_z w_y$ give rise to vortex tilting. The fourth term $-d\omega$ describes damping effect that has the same dissipation time as the zonal momentum, and its value is proportional to the vorticity ω instead of PV.

On the mesoscale, the vertical velocity w is directly balanced by the diabatic heating S^θ in the M-ITCZ equations, whose vertical gradient also means wind divergence and convergence due to the conservation of volume in Eq.1d. Meanwhile, the momentum damping d in Eqs.1a-1b for cumulus drag has increasing dissipation time scale as height increases (Romps 2014), which tends to decelerate winds and restore the forced flows into equilibrium. Therefore, the M-ITCZ equations with the prescribed diabatic heating profile is a forced and damped model.

The conservation of kinetic energy can provide a better understanding of the dynamical field, especially the acceleration/deceleration effects due to the upscale impact of the mesoscale fluctuations. In details, the conservation of kinetic energy on the mesoscale can be derived by multiplying the zonal momentum equation in Eq.1a by u and the meridional momentum equations in Eq.1b by v and adding these two equations together as follows,

$$\frac{\partial K_m}{\partial t} + \nabla \cdot (K_m \mathbf{v} + p\mathbf{u}) = -\frac{\partial \Pi}{\partial X} u - 2dK_m, \tag{8}$$

where $\mathbf{v} = (u, v, w)$ represents three-dimensional velocity field and $\mathbf{u} = (u, v, 0)$ represents horizontal velocity field. $K_m = \frac{u^2+v^2}{2}$ denotes kinetic energy of horizontal flow field on the mesoscale. Eq.8 is in the general form of the conservation of energy, which includes the time tendency of kinetic energy, the kinetic energy fluxes and some source terms on the right hand side. Specially, the kinetic energy flux term $K_m\mathbf{v}$ involves the three-dimensional flow field, while only horizontal flows do work against pressure force in the term $p\mathbf{u}$. The first term $-\Pi_X u$ on the right hand side of Eq.8 represents the acceleration/deceleration effects of the planetary-scale pressure perturbation in the zonal direction. The second term $-2dK_m$ represents the energy dissipation due to cumulus drag, which has half dissipation time scale as momentum dissipation.

On the planetary scale, after multiplying Eq.6a by $\bar{u}$, the equation for kinetic energy of zonal winds can be obtained as follows,

$$\frac{\partial}{\partial t}\left(\frac{\bar{u}^2}{2}\right)+\frac{\partial}{\partial y}\left(\bar{v}\frac{\bar{u}^2}{2}\right)+\frac{\partial}{\partial z}\left(\bar{w}\frac{\bar{u}^2}{2}\right)=y\bar{v}\bar{u}-\frac{\partial \Pi}{\partial X}\bar{u}-d\bar{u}^2+F^u\bar{u}, \tag{9}$$

where $F^u=-\left(\overline{v'u'}\right)_y-\left(\overline{w'u'}\right)_z$ is the eddy flux divergence of zonal momentum from the mesoscale fluctuations. Similarly, the equation for kinetic energy of meridional winds can also be obtained by using Eq.1b and multiplying $\bar{v}$,

$$\frac{\partial}{\partial t}\left(\frac{\bar{v}^2}{2}\right)+\frac{\partial}{\partial y}\left(\bar{v}\frac{\bar{v}^2}{2}\right)+\frac{\partial}{\partial z}\left(\bar{w}\frac{\bar{v}^2}{2}\right)=-y\bar{v}\bar{u}-\frac{\partial \bar{p}}{\partial y}\bar{v}-d\bar{v}^2+F^v\bar{v}, \tag{10}$$

where $F^v=-\left(\overline{v'v'}\right)_y-\left(\overline{w'v'}\right)_z$ is the eddy flux divergence of meridional momentum from the mesoscale fluctuations. By adding Eq.9-10 together, the equation for the total kinetic energy reads as follows,

$$\frac{\partial K}{\partial t}+\frac{\partial}{\partial y}(\bar{v}K)+\frac{\partial}{\partial z}(\bar{w}K)=-\frac{\partial \Pi}{\partial X}\bar{u}-\frac{\partial \bar{p}}{\partial y}\bar{v}-2dK+F^u\bar{u}+F^v\bar{v}, \tag{11}$$

where $K=\frac{\bar{u}^2+\bar{v}^2}{2}$represents the kinetic energy of horizontal flow.

Eq.11 describes the budget of horizontal kinetic energy on the planetary scale, including the time tendency of kinetic energy and the kinetic energy fluxes in the meridional/vertical directions on the left hand side, and some source terms on the right hand side. The kinetic energy flux term $(\bar{v}K)_y+(\bar{w}K)_z$ represents the advection effect of the planetary-scale meridional/vertical circulation $(\bar{v},\bar{w})$. On the right hand side, the first term $-\Pi_X\bar{u}$ represents the acceleration/deceleration effects of large-scale pressure gradient in zonal direction. The second term $-\bar{p}_y\bar{v}$ represents the acceleration/deceleration effects of pressure gradient in meridional direction. The third term $-2dK$ describes the energy dissipation due to cumulus drag, which has half dissipation time scale as momentum dissipation. The last two terms, $F^u\bar{u}+F^v\bar{v}$, denote the acceleration/deceleration effects due to mesoscale eddy flux divergence of zonal and meridional momentum. Furthermore, the first terms $\mp y\bar{v}\bar{u}$ on the right hand side of Eq.9-10 cancel each other and do not show up in the kinetic energy equation in Eq.11. In fact, these two terms represent energy transfer between the planetary-scale zonal and meridional velocity due to the Coriolis force.

3. ITCZ Breakdown in Zonally Symmetric Planetary-Scale Flow

The eastern Pacific ITCZ turns out to be an unstable environment where many tropical cyclones are generated (Gray 1979). One case of the ITCZ breakdown in the eastern Pacific is observed in July of 1988 (Ferreira and Schubert 1997), based on geostationary operational environmental satellites (GOES) infrared (IR) images. In that case, the ITCZ was first seen as an elongated zonal band of cloudiness off the equator in the eastern Pacific. After two days, the ITCZ started undulating and breaking down into several tropical cyclones, which moved into high latitudes, followed by the reforming of the ITCZ cloud band in its original location. The atmospheric flows over the eastern Pacific are organized into a hierarchical structure across multiple spatiotemporal scales. Such hierarchical structure of convective and dynamical fields is a suitable scenario to use multi-scale models (Majda 2007).

After the ITCZ breakdown, the resulting tropical cyclones are typically accompanied by upward motion and cloud clusters over several hundred kilometers (Mapes and Houze Jr 1993). Meanwhile, the large-scale meridional circulation including Pacific easterly waves over the eastern Pacific has zonal extent of several thousand kilometers (Serra et al. 2008). On the other hand, the M-ITCZ equations describe such multi-scale features across two zonal spatial scales (planetary-scale $L_p = 5000$ km, mesoscale $L_m = 500$ km), which match well with the typical length scale of small-scale tropical cyclones and the large-scale meridional circulation, justifying the appropriateness of using the M-ITCZ equations to model the ITCZ breakdown and its upscale impact on the planetary-scale circulation. Over the eastern Pacific, the large-scale meridional circulation has zonal variation due to boundary conditions such as sea surface temperature gradient and atmospheric disturbance such as easterly waves (Toma and Webster 2010a,b). In order to model ITCZ breakdown in a simple scenario, the solutions of the M-ITCZ equations are assumed to be zonally symmetric on the planetary scale so that all derivatives about planetary-scale X vanish. Then the M-ITCZ equations in Eqs.1a-1g are reduced to the MEWTG equations in Eqs.4a-4d, where S^θ stands for thermal forcing such as diabatic heating in cloud clusters and radiative cooling effects.

For simplicity, local periodicity is imposed in mesoscale zonal direction and rigid-lid boundary conditions are imposed in meridional and vertical boundaries. By taking both zonal and meridional averaging and enforcing the boundary conditions in these two directions, Eq.4d reduces to $\langle \bar{w} \rangle_z = \langle \bar{S}^\theta \rangle_z = 0$, which means conservation of volume at each level. Since vertical velocity vanishes in the rigid-lid vertical boundaries, an implicit constraint for diabatic heating can be derived as follows,

$$\left\langle \bar{S}^\theta \right\rangle = 0, \tag{12}$$

where the notation bar and angle bracket stand for mesoscale zonal and meridional averaging as defined in Eqs.2-3.

The momentum dissipation for cumulus drag in the convective region is described by a linear damping law in Eqs.4a-4b. The coefficient d in units of $1/day$ sets the time scale for momentum dissipation on the mesoscale. According to the observation, momentum damping time scale at the surface of the Pacific ocean could be as strong as 1 day (Deser 1993) while that at the upper troposphere is much longer. In general, the momentum damping of large-scale circulation occurs on a time scale of $\mathcal{O}(1-10)$ days, and also depends on the vertical wavelength of the wind profile (Romps 2014). For simplicity, the momentum damping coefficient d is assumed to be a linear function of height $d(z)$, which has 1 day damping time scale at surface and 10 days damping time scale at top of the troposphere.

Eqs.4a-4d are solved numerically by using a new method based on the Helmholtz decomposition and a second-order corner transport upwind scheme to effectively resolve the non-linear eddies. The details of the numerical scheme are summarized in Appendix.

For the numerical simulations in Sec.4, the banded region from $15°S$ to $15°N$ circling the globe in the tropics is chosen as the full domain with zonal extent $0 \le X \le 40 \times 10^3 km$. As summarized in Appendix, the coarse grid number N_{xp} is fixed and the zonal extent of each mesoscale box is $0.976 \times 10^3 km$, which is in the same order as the mesoscale length, $L_m = 500km$. In the numerical scheme with nested grids, each coarse cell corresponds to a single mesoscale box with horizontal extent $0 \le x \le 0.976 \times 10^3 km, -1.5 \times 10^3 km \le y \le 1.5 \times 10^3 km$ and the vertical extent $0 \le z \le 15.7km$. Besides, the planetary-scale domain and all mesoscale domains share the same vertical grids. The details about grid numbers and grid spacing in the numerical simulations are summarized in Table.1 and Sec.4. Here the planetary-scale variations are ignored and a relatively high spatial resolution for a single mesoscale domain is chosen to resolve mesoscale eddies in the MEWTG equations. A short time step is used for numerical accuracy and stability.

a. Deep and shallow heating profile

The dominating meridional circulation over the eastern Pacific consists of a strong overturning circulation cell around the equator and a weak one at high latitudes of the Northern Hemisphere. The strong overturning cell around the equator expands over the whole troposphere with southerly winds in its lower branch near the surface and northerly winds in its upper branch near the tropopause, which is referred to deep meridional circulation. Such deep overturning cell can be explained as the response of the large-scale circulation to deep convective heating in the ITCZ (Schneider and Lindzen 1977; Wu 2003). The deep convective heating in the ITCZ comes from latent heat release during precipitation associated with cloudiness such as deep convective cumulonimbus clouds, which tends to warm and dry the entire troposphere and produce amounts of rainfall.

Here the deep convective heating S^{θ} for a single cloud cluster in dimensionless units is prescribed as follows,

$$S^{\theta} = cH(x,y)\,G(z)\,\phi(t)\,, \tag{13}$$

where heating magnitude coefficient $c = 2$ corresponds to the maximum heating rate $66K \cdot day^{-1}$. $H(x,y)$ is the horizontal envelope function shown in Fig.1a. The vertical heating profile is the first baroclinic mode $G(z) = \sin(z)$, as shown in Fig.1c. $\phi(t)$ is the time dependent heating magnitude, which linearly increases from 0 to 1 at day 1 and remains constant afterwards. Since the typical life time of cloud clusters is between several hours to several days (Mapes and Houze Jr 1993), here 1 day in duration is set as initialization time when the deep convective heating increases from zero to its maximum magnitude. The prescribed diabatic heating S^{θ} is used to mimic convective heating associated with a single deep cloud cluster in the ITCZ. As shown in Fig.1a, the deep heating is located at the latitudes between $y = 0km$ and $y = 1.2 \times 10^{3}km$ of the Northern Hemisphere and zonally localized in the center of the mesoscale domain. Outside of the convective heating region such as the Southern Hemisphere and high latitudes of the Northern Hemisphere, there is horizontally uniform cooling in much weaker magnitude, which is used to mimic radiative cooling in the troposphere.

The shallow meridional circulation is also significant in the meridional circulation over the eastern Pacific, besides the deep meridional circulation. The existence of shallow meridional circulation is beyond the classic theory of the Hadley circulation over the eastern Pacific, where deep convection typically dominates and drives meridional circulation with deep vertical extent. By analyzing observational data from upper-air soundings, aircraft dropsondes and wind profilers (Zhang et al. 2004), the shallow meridional circulation is identified as a circulation cell with its northerly cross-equatorial return flow above the atmospheric boundary layer from the ITCZ into the Southern Hemisphere. The causes and dynamics of the shallow meridional circulation are explained by a large-scale sea-breeze circulation theory and an idealized Hadley circulation simulation driven by moist convection in a tropical channel (Nolan et al. 2007).

As suggested by many theoretical studies (Schneider and Lindzen 1977; Gill 1980; Wu 2003), the large-scale tropical circulation can be regarded as the response to convective heating associated with tropical precipitation. Correspondingly, the diabatic heating associated with the shallow meridional circulation has shallower vertical extent than that of deep convective heating. Here the shallow congestus heating S^{θ} in dimensionless units is prescribed in the same general expression in Eq.13, and heating magnitude coefficient c_s is 1 (maximum heating rate $33K\cdot day^{-1}$). The horizontal profile $H(x,y)$ and time series $\phi(t)$ are the same as Eq.13. The vertical profile of shallow congestus heating $G(z)$ is prescribed in Fig.1c and reaches its maximum value around the height $z=4$ km , while that of deep convective heating reaches maximum value at the height $z=7.8$ km. According to the conservation of volume in Eq.4d, horizontal wind divergence is proportional to the gradient of $G(z)$ as shown in Fig.1c. Firstly, the magnitude of wind convergence at the surface in the shallow congestus heating case is more than twice as much as that in the deep convective heating case. Secondly, compared with the deep convective heating case, the maximum wind divergence in the shallow heating case is near the height $z=6$ km, which qualitatively matches well with the returning flows above the atmospheric boundary layer in the shallow meridional circulation (Zhang et al. 2004).

In the following discussion, two deep heating cases are considered. The strong deep heating case (*deep2*: magnitude coefficient $c = 2$) indicates the significant baroclinic aspects of ITCZ breakdown. The relatively weak deep heating case (*deep1*: magnitude coefficient $c = 1$) in the same maximum heating magnitude as the shallow heating is used for comparison with the shallow heating case. According to Fig.1d, the spin up time for all the scenarios is around 3 days, here the numerical solutions at day 4 are mainly chosen for discussion.

b. Formation and undulation of a positive vorticity strip

In the ITCZ, convective activities occur with large amounts of rainfall, which release latent heat and lift air parcels to higher levels. Due to the conservation of mass, such upward motion of air leads to wind convergence (divergence) in the lower (upper) troposphere. Under the Coriolis force, the southerly (northerly) winds to the south (north) of the ITCZ in the Northern Hemisphere deflect to the right side and generate westerly (easterly) winds, resulting in meridional shear of zonal winds in the lower troposphere. Such meridional shear of zonal winds is characterized by a positive vorticity strip in the Northern Hemisphere. Therefore, the ITCZ breakdown can be visualized through the vorticity strip dynamics from its formation and undulation in the early stage to its breakdown into several vortices later. In this section, such a scenario involving a positive vorticity strip is captured.

Fig.2a-c shows the horizontal profile of velocity and vorticity fields at the surface during the first 4 days in the *deep2* heating case. At day 1 in Fig.2a when the magnitude of diabatic heating reaches its maximum, a positive low-level vorticity strip develops on the poleward side of the diabatic heating region. It is centered at the latitude $y = 750km$. As explained above, such a positive vorticity strip with meridional shear of zonal winds is related to wind convergence in the low troposphere and meridional wind deflection due to the Coriolis force. Meanwhile, the positive vorticity has nearly zonally uniform strength along all longitudes of the diabatic heating region. At the lower latitudes of the Northern Hemisphere, southerly winds deflect to the right side due to the Coriolis force and generate westerly wind anomalies. Stronger westerly winds are generated as the Coriolis coefficient increases on the equatorial β-plane. Therefore, such positive meridional shear of zonal velocity induces negative vorticity anomalies at low latitudes of the Northern Hemisphere. Besides, winds in the Southern Hemisphere blow from the southeast, which has similar wind direction and magnitude as the trade winds (Wyrtki and Meyers 1976). At day 2 in Fig.2b, the magnitude of the positive vorticity strip in the Northern Hemisphere gets strengthened. The zonally elongated vorticity strip starts to undulate with its eastern end moving northward and western end moving southward, which is reminiscent of the undulation process of cloudiness during the ITCZ breakdown. Besides, negative vorticity anomalies at low latitudes of the Northern Hemisphere have stronger magnitude and broader zonal extent. The horizontal flow field has increasing maximum wind magnitude but its horizontal spatial pattern is similar to Fig.2a. At day 4 in Fig.2c, the magnitude of the positive vorticity strip continuously increases and its maximum value reaches about $16day^{-1} \approx 1.85 \times 10^{-4}s^{-1}$, which is comparable with the observational data as well as numerical simulations (Ferreira and Schubert 1997). As both ends of the positive vorticity strip undulate in weak magnitude, a strong positive vortex forms in the middle, resembling the formation of tropical cyclones. In addition, such a positive vorticity strip is surrounded by negative vorticity anomalies in both its northern and southern sides. Although the maximum wind strength still increases, the spatial pattern of horizontal flow field is quite similar to that in the early stage.

One interesting phenomenon with regard to the numerical solutions in Fig.2a-c is that the zonally elongated positive vorticity strip is located in the northern side of the diabatic heating region. The underlying mechanism can be explained as follows. First, as far as the mesoscale zonal mean flow is concerned, the conservation of volume is guaranteed through the divergence-free meridional circulation in Eq.4d,

$$\frac{\partial \bar{v}}{\partial y} + \frac{\partial \bar{w}}{\partial z} = 0, \tag{14}$$

Considering the fact that there are a strong circulation cell around the equator and a weak circulation cell in the Northern Hemisphere, the southerly winds in the lower branch of the strong circulation cell are prevailing in the Southern Hemisphere and low latitudes of the Northern Hemisphere, and vanishing at the latitude where upward and downward motion to its south exactly cancel by each other. Since downward motion to the south of the diabatic heating region occurs in much broader area than that to the north, the latitude where meridional winds vanish is located in the northern side of the diabatic heating region, generating negative meridional shear of zonal winds (positive vorticity anomalies $\omega = v_x - u_y$). Secondly, PV ($Q = \omega + y$) is advected by three-dimensional flow and forced by several terms involving gradient of diabatic heating as well as damping in Eq.7. Since meridional winds converge in the Northern Hemisphere, the vorticity ω decreases (increases) due to the increasing (decreasing) mean PV y to the south (north), resulting in poleward displacement of positive vorticity anomalies.

The other interesting phenomenon arising in the numerical solutions in Fig.2a-c is the undulation of the positive vorticity strip and the resulting strong positive vortex in its middle, which describes a similar scenario for the ITCZ breakdown. According to the conservation of volume in Eq.4d, horizontal wind convergence is induced by the accelerating upward motion in the lower troposphere in the heating region. Due to the Coriolis force, the southerly (northerly) winds to the south (north) of the ITCZ deflect to the right side, which then become southwesterly (northeasterly) winds. The overall flow field near the diabatic heating region tends to rotate counterclockwise, and advect the eastern (western) end of the positive vorticity strip poleward (equatorward) as shown in Fig.2b-c

. Such undulation of the positive vorticity strip in the rotational flows due to the zonal asymmetry and the Coriolis force is related with the 'vortex roll-up' mechanism, which is one of the main mechanisms used to explain the eastern Pacific ITCZ breakdown (Hack et al. 1989; Ferreira and Schubert 1997; Wang and Magnusdottir 2005).

The vertical structure of the deep heating in Fig.1c reaches maximum value in the middle troposphere at height $z = 7.48$ km. Fig.2e-g shows the horizontal profile of velocity and vorticity field in the middle troposphere during the first 4 days in the *deep2* heating case. A positive vorticity strip is generated in the northern side of the diabatic heating region, gets strengthened at day 2 in Fig.2f, undulates and breaks down into a strong vortex in the middle at day 4 in Fig.2g. Besides, a pair of vortex dipoles form at low latitudes of the Northern Hemisphere with negative (positive) vorticity anomalies to the east (west). Such vortex dipoles can be explained through the PV equation in Eq.7, where PV anomalies are forced by the vorticity tilting term $-v_z S_x^\theta$. The low latitudes of the Northern Hemisphere is dominated by southerly winds in the lower troposphere and northerly winds in the upper troposphere, indicating negative vertical shear of meridional velocity. On the other hand, zonal gradient of diabatic heating is negative (positive) to its eastern (western) end. Therefore, the product term $-v_z S_x^\theta$ have negative (positive) value to the eastern (western) end of the diabatic heating region, resulting in a pair of vortex dipoles with negative (positive) anomalies to the east (west). As far as the velocity field is concerned, the strong positive vortex in the northern side of the diabatic heating and the western vortex dipole come along with cyclonic flows, while the eastern vortex dipole comes along with anticyclonic flows. In the Southern Hemisphere, the prevailing westerly winds in gradually increasing wind strength, and the maximum westerly wind occurs at the latitude $y = -10^3$ km.

Horizontal flows at the top diverge over the deep heating region and move northward and southward afterwards. Fig.2i-k shows the horizontal profile of velocity and vorticity fields near the top of the troposphere during the first 4 days in the *deep2* heating case. As a counterpart of the positive vorticity strip at surface, a negative vorticity strip is generated in the Northern Hemisphere. Since PV is advected by the three-dimensional flow in Eq.7, this negative vorticity strip has broader meridional extent and weaker magnitude due to the advection effects of meridionally divergent winds. As far as the velocity field is concerned, the strong meridional shear of westerly winds at high latitudes of the Southern Hemisphere results in strong vorticity anomalies near the southern boundary. Since the momentum damping strength at the top of the domain is only 1/10 of that at surface, the maximum wind magnitude at the top is much stronger than those at lower levels.

Compared with the deep convective heating in Fig.1c, shallow congestus heating has stronger vertical gradient near the surface when the maximum heating magnitudes are the same. Such large vertical gradient of upward motion also means stronger horizontal wind convergence at the surface, which can accelerate the ITCZ breakdown as shown in the other study (Wang and Magnusdottir 2005).

Fig.3a-c shows the horizontal profile of velocity and vorticity fields at the surface in the first 4 days in the shallow heating case. The velocity and vorticity fields share many similar features with those in the deep convective heating case in Fig.2a-c, including the formation and undulation of a positive vorticity strip. In spite of the similarity, a direct comparison is not appropriate since the maximum shallow congestus heating is $33Kday^{-1}$ while the maximum deep convective heating is $66Kday^{-1}$. Fig.3d-f shows the horizontal profile of velocity and vorticity fields at the surface in the *deep1* heating case with maximum heating magnitude $33Kday^{-1}$. In contrast, there are no significant positive vorticity anomalies in the middle of the positive strip after 4 days. As for the horizontal wind field, both cases with deep/shallow heating share similar spatial patterns with cyclonic flows in the Northern Hemisphere, southerly winds around the equator and southeasterly winds in the whole Southern Hemisphere, but the maximum wind strength in the *deep1* heating case in Fig.3d-f is about half that in the shallow heating case in Fig.3a-c. In fact, such stronger horizontal velocity and vorticity fields in the shallow heating case have been emphasized in a model for hot towers in the hurricane embryo (Majda et al. 2008) and the ITCZ breakdown in three-dimensional flows (Wang and Magnusdottir 2005).

Different from the deep convective heating case, the velocity and vorticity fields in the shallow heating case are confined in the lower troposphere. Fig.3g-i shows the horizontal profile of velocity and vorticity field at height $z = 7.48$ km in the shallow heating case. Again, the overall spatial pattern of the velocity and vorticity fields is quite similar to that in the deep convective heating case with doubled magnitude in Fig.2i-k. Over the diabatic heating region in the Northern Hemisphere, divergent winds prevail and negative vorticity anomalies have broader meridional extent. The whole Southern Hemisphere is dominated by zonally uniform westerly winds with the maximum wind magnitude at $y = 10^3$ km, resulting in positive meridional shear of zonal winds (negative vorticity) near the southern boundary.

c. Vertical stretching of wind and vorticity fields

Deep clouds such as cumulonimbus have vertical extent throughout the whole troposphere, warm and dry the entire troposphere, contributing the majority of tropical rainfall (Khouider and Majda 2008). During convective periods associated with deep clouds in the ITCZ, warm and moist air parcels have enough buoyancy to get lifted up from the atmospheric boundary layer to the upper troposphere. Besides, the upward motion in the ITCZ has significant wind strength in the free troposphere, and it serves to transport energy and moisture from the lower troposphere to the upper troposphere. In contrast, shallow meridional circulation is characterized by a northerly return flow just above the atmospheric boundary layer (Zhang et al. 2004). In the northern branch of the overturning circulation cell, the upward motion over the eastern Pacific ITCZ is driven by shallow congestus heating, which is confined in the lower troposphere. On the other hand, the MEWTG equations in Eqs.4a-4d are fully nonlinear with the thee-dimensional advection effects. Considering that vertical velocity is directly balanced by diabatic heating in Eq.4c, persistent upward motion exists in the diabatic heating regions, advecting both horizontal velocity and vorticity field upward and resulting in the vertical stretching of these fields.

Fig.4a-c shows the vertical profile of horizontal velocity and vorticity fields along the latitude $y = 0.8 \times 10^3$ km at day 4 in the *deep2* heating case. As shown in Fig.4c, a positive vorticity disturbance is located in the middle longitude of the mesoscale domain with its maximum magnitude at the surface. Due to persistent upward motion in the diabatic heating region, the positive vorticity, which characterizes cyclonic flows following the ITCZ breakdown, extends to the upper troposphere. As far as the horizontal flow field in Fig.4a-b is concerned, the cyclonic flows associated with the positive vortex also stretch vertically over the whole troposphere and their vertical structure becomes dominated by the barotropic mode. Fig.4d-f shows the same fields in the shallow heating case. Both velocity and vorticity fields are confined to the much shallower levels compared with those in the deep heating case. Since the positive vorticity anomalies are accompanied by cyclonic flows, southerly winds to the east of the positive vortex and northerly winds to the west can be found in Fig.4e. Besides, the positive vorticity anomalies in the middle are surrounded by weak negative vorticity anomalies to both the east and west as well as the top.

Along with the vertical stretching of positive vorticity anomalies, winds diverge in the upper levels and go along the upper branches of the overturning circulation cells. Fig.4g-i shows the vertical profile of horizontal velocity and vorticity field along the longitude $x = 0.43 \times 10^3 km$ at day 4 in the *deep2* heating case. As indicated by Fig.4i, positive vorticity anomalies have very narrow meridional extent but deep vertical extent, which are accompanied by horizontal cyclonic flows, including westerly winds to the south of the positive vortex and easterly winds to the north as shown in Fig.4g. A strong circulation cell forms around the equator and a weak one forms at high latitudes of the Northern Hemisphere, whose upper and lower branches of meridional winds are shown in Fig.4h. Fig.4j-l shows the same fields in the shallow heating case. The overall spatial pattern of velocity and vorticity fields is similar to those in deep convective heating case, except that the vertical extent is much shallower. As shown by Fig.4l, the positive vorticity vortex is located to the north of the diabatic heating region and surrounded by weak negative vorticity anomalies. The shallow congestus heating can also drive a strong overturning circulation cell around the equator and a weak circulation cell at high latitudes of the Northern Hemisphere. The corresponding lower and upper branches of these overturning circulation cells are shown in Fig.4k. Due to the strong momentum dissipation in lower levels, the resulting maximum zonal winds in the shallow heating case are much weaker than those in the deep convective heating case.

d. Eddy flux divergence of zonal momentum and mean flow acceleration/deceleration

The M-ITCZ equations are a multi-scale model with two spatial zonal scales (planetary-scale $L_p = 5000$ km, mesoscale $L_m = 500$ km). This scale selection is a good approximation for the hierarchical structure of tropical convection across multiple spatiotemporal scales in the ITCZ (Majda and Klein 2003; Majda 2007). Eddy flux divergence of zonal momentum arising from the mesoscale dynamics forces the planetary-scale circulation, while the large-scale flow field provides the background mean flow for the mesoscale dynamics. Specifically, the planetary-scale zonal momentum equation is derived by taking mesoscale zonal averaging on Eq.4a as follows,

$$\frac{\partial \bar{u}}{\partial t} + \bar{v}\frac{\partial \bar{u}}{\partial y} + \bar{w}\frac{\partial \bar{u}}{\partial z} - y\bar{v} = -d\bar{u} - \frac{\partial}{\partial y}\left(\overline{v'u'}\right) - \frac{\partial}{\partial z}\left(\overline{w'u'}\right), \tag{15}$$

where the notation bar is defined in Eq.2 and the prime denotes mesoscale fluctuations. Eq.15 describes zonal momentum dynamics on the planetary-scale, which can be used to model zonal jets associated with the meridional circulation over the eastern Pacific. In detail, the planetary-scale zonal velocity is advected by the two-dimensional planetary-scale meridional circulation $(\bar{v}, \bar{w})$ and forced by the Coriolis force and linear momentum damping. Besides, the eddy flux divergence of zonal momentum that involves mesoscale fluctuations appears on the right hand side of Eq.15 and represents upscale impact of mesoscale fluctuations on the planetary-scale circulation. In fact, the eddy flux divergence of zonal momentum is referred to convective momentum transport (CMT), which has been studied from different perspectives to highlight its significance such as stochastic models (Majda and Stechmann 2008; Khouider et al. 2012) and dynamical models with cloud parameterization (Majda and Stechmann 2009). This eddy flux divergence of zonal momentum in dimensionless units reads as follows,

$$F^U = -\frac{\partial}{\partial y}\left(\overline{v'u'}\right) - \frac{\partial}{\partial z}\left(\overline{w'u'}\right), \tag{16}$$

The eddy flux divergence of zonal momentum F^U in Eq.16 constitutes an upscale zonal momentum forcing on the planetary scale that can have a significant impact on the planetary-scale flow. Specifically, positive (negative) anomalies of eddy flux divergence of zonal momentum F^U represent eastward (westward) momentum forcing. Fig.5a-c shows eddy flux divergence of zonal momentum F^U in the latitude-height diagram at day 4 in the *deep2* heating case. Along the latitude where the positive vortex located (see Fig.4i), eastward momentum forcing is induced by eddy flux divergence of zonal momentum F^U with deep vertical extent, which is mainly contributed by the meridional component of F^U in Fig.5b. In addition, meridionally alternating eastward and westward momentum forcing exists at low latitudes and the middle troposphere of the Northern Hemisphere in Fig.5a, which is directly related to the vorticity dipoles as shown in Fig.2g. Lastly, the maximum magnitudes of both the meridional and vertical components of F^U are comparable to each other, providing significant contributions to the total eddy flux divergence of zonal momentum. Fig.5d-f shows the same fields in the shallow heating case. The most significant F^U anomalies are similar to those in the *deep2* heating case but confined in the lower troposphere. Besides the positive anomalies at high latitudes of the Northern Hemisphere, there are also significant negative anomalies to the south of the positive anomalies near the surface. At low latitudes of the Northern Hemisphere at height $z = 4$ km, the eddy flux divergence of zonal momentum has significant anomalies with eastward momentum forcing on top of westward momentum forcing in upward/equatorward tilt. The magnitudes of momentum forcing in the meridional and vertical components are comparable but their spatial patterns are quite different in this region. In order to compare the eddy flux divergence of zonal momentum, Fig.5g-i shows the same fields in the *deep1* heating case. The magnitudes of total eddy flux divergence of zonal momentum and its meridional and vertical components are much weaker than those in the shallow heating case in Fig.5d-f, highlighting the significant upscale impact in the shallow heating case.

As indicated by Eq.15, eddy flux divergence of zonal momentum arising from the mesoscale dynamics further forces the planetary-scale circulation and induces zonal jet anomalies. Its impact can be illustrated through the comparison between numerical solutions with and without the eddy momentum forcing F^U. Instead of utilizing the mesoscale zonally localized diabatic heating in Fig.1a, a mesoscale zonally uniform heating profile is prescribed in the same expression in Eq.13, but its horizontal envelope function $H(y)$ is replaced by the one in Fig.1b with the same zonal mean. The differences of mesoscale zonal mean of zonal velocity reflect the impact of eddy flux divergence of zonal momentum on the planetary-scale circulation. Fig.6a-b shows mean zonal velocity $\bar{u}$ in the latitude-height diagram at day 4 in the zonally localized and uniform *deep2* heating case. The mean zonal velocity fields in both these two cases share several common features, which are consistent with a strong overturning circulation cell around the equator and a weak circulation cell in the Northern Hemisphere. In particular, the horizontal profiles of velocity and vorticity fields at different levels in the zonally uniform heating case are shown in panels (d,h,l) of Fig.2. Although the maximum magnitude of zonal wind anomalies due to eddy flux divergence of zonal momentum in Fig.6c is about $\frac{1}{10}$ of that in Fig.6a-b, most of these zonal wind anomalies are localized in places where the mean zonal wind is relatively weak, resulting in significant rectification of zonal jets. Particularly, there are westerly wind anomalies along the latitude of the positive vortex (see Fig.4i), which matches well with the eastward momentum forcing in the same region in Fig.5a. Due to the advection effect of the mean meridional circulation $(\bar{v}, \bar{w})$, such eastward zonal wind anomalies extend to the upper troposphere, the equator and the Southern Hemisphere. Besides, meridionally alternate zonal wind anomalies in the middle troposphere and low latitudes of the Northern Hemisphere match well with the spatial pattern of the eddy flux divergence of zonal momentum in Fig.5a. Fig.6d-f shows the same fields in the shallow heating case. The overall spatial patterns of mean zonal velocity and zonal velocity anomalies are mostly confined in the shallower levels. The mean zonal velocity in Fig.6d shares many common features as that in the mesoscale zonally uniform heating case in Fig.6e. The spatial pattern of mean zonal wind anomalies in Fig.6f is consistent with that of eddy flux divergence of zonal momentum in Fig.5d. There are westerly wind anomalies along the latitude $y = 800$ km where the positive vortex is located (see Fig.4l) and easterly wind anomalies to the south of the westerly wind anomalies in the lower troposphere. Zonal wind anomalies with westerlies on top of easterlies occur at low latitudes of the Northern Hemisphere.

The eddy flux divergence of zonal momentum in Eq.16 is a crucial quantity, because it not only significantly modifies the zonal momentum budget as momentum forcing, but also involves energy transfer across multiple spatial scales and induces acceleration/deceleration effects on the planetary-scale mean flow. Here the acceleration and deceleration of eddy flux divergence of zonal momentum is investigated through the kinetic energy of zonal winds in Eq.9 instead of the total kinetic energy in Eq.11. One essential reason is that only the mesoscale mean zonal velocity is coupled with the planetary-scale gravity waves in Eqs.6a-6f, while the mean meridional velocity is directly balanced by the diabatic heating through Eqs.6b-6c. The equation for kinetic energy of mean zonal velocity is reduced from Eq.9,

$$\frac{\partial K^u}{\partial t} + \frac{\partial}{\partial y}(\bar{v}K^u) + \frac{\partial}{\partial z}(\bar{w}K^u) = y\bar{v}\bar{u} - 2dK^u + F^u\bar{u}, \tag{17}$$

where $K^u = \frac{\bar{u}^2}{2}$ represents kinetic energy of planetary-scale zonal winds.

The eddy energy transfer term $F^u\bar{u}$ in Eq.17 is a product of eddy flux divergence of zonal momentum F^U and mean zonal velocity $\bar{u}$, which can be interpreted as acceleration/deceleration effects of F^u on the mean zonal winds. If the sign of the term $F^u\bar{u}$ is positive (negative), the kinetic energy of zonal winds tends to increase (decrease) and the eddy energy transfer term $F^u\bar{u}$ induces acceleration (deceleration) effects. Besides, the magnitude of acceleration/deceleration effects of the eddy energy transfer $F^u\bar{u}$ depends on the magnitudes of both eddy flux divergence of zonal momentum F^u and mean zonal velocity $\bar{u}$. Fig.7a shows acceleration/deceleration effects of eddy flux divergence of zonal momentum at day 4 in the *deep2* heating case. Along the latitude where the positive vortex is located (see Fig.4i), the acceleration effects are induced by eastward momentum forcing F^u on the westerly mean flows $\bar{u}$. To both the northern and southern sides of that acceleration effects, the deceleration effects with narrow meridional extent is mostly significant in the lower troposphere, which decelerate the westerly (easterly) winds to the south (north) of the positive vortex. At low latitudes of the Northern Hemisphere, acceleration effects are also significant in the middle troposphere where mean zonal winds are weak in Fig.6b and modified mainly by eddy flux divergence of zonal momentum in Fig.5a. Fig.7b shows the acceleration/deceleration effects due to eddy flux divergence of zonal momentum in the shallow heating case. The most significant acceleration/deceleration effects are confined in the lower troposphere.

Besides the acceleration effects at high latitudes, there are also deceleration effects of westward (eastward) eddy flux divergence of zonal momentum on the mean westerly (eastward) winds to the south (north) of the latitude $y = 800$ km. Such lower-level deceleration effects in the diabatic heating region is typically seen in other studies about CMT (Majda and Stechmann 2008, 2009). As a clear comparison, the eddy energy transfer $F^u\bar{u}$ in the *deep1* heating case in Fig.7c is much weaker than that in the shallow heating case in Fig.7b, highlighting the significant upscale impact of mesoscale fluctuations in the shallow congestus heating in terms of kinetic energy budget.

4. ITCZ Breakdown in Zonally Varying Planetary-Scale Flow

In this section, the M-ITCZ equations are utilized to simulate the ITCZ breakdown process over the eastern Pacific involving both the mesoscale and planetary-scale dynamics. In each mesoscale cell, periodic boundary conditions are imposed in the zonal direction and rigid-lid boundary conditions are imposed in the meridional and vertical directions. On the planetary scale, the zonal periodic boundary condition is naturally consistent with the belt of tropics around the globe. In addition, the model setup and numerical details such as mesoscale and planetary-scale domain size, spatial and temporal resolutions are exactly the same as Sec.3. Lastly, the whole model is driven by diabatic heating on both mesoscale and planetary scale, and all physical variables are initialized from a background state of rest. The whole domain is discretized with nested coarse and fine grids as shown in Fig.8. In the numerical simulations, the MEWTG equations in Eqs.4a-4d are only valid on each mesoscale box with the zonally periodic boundary conditions. After taking zonal averaging of physical variables in each mesoscale domain, the planetary-scale physical quantities on each coarse grid is obtained and further involved in the planetary-scale gravity waves. More numerical details are summarized in Appendix.

In the ITCZ, the diabatic heating can be released during tropical precipitation in cloud clusters. In order to model the ITCZ over the eastern Pacific, diabatic heating S^θ is modulated by a planetary-scale zonally localized envelope. In general, such a two-scale diabatic heating S^θ in dimensionless units reads as follows,

$$S^\theta = cF(X)H(x,y)G(z)\phi(t), \tag{18}$$

where $F(X) = 1.2e^{-(X-4)^2}$ is the planetary-scale envelope function , $H(x,y)$ is the horizontal heating profile, which can be either mesoscale zonally localized heating in Fig.1a or uniform heating in Fig.1b. $G(z)$ is the vertical heating profile, which can have either deep or shallow vertical extent in Fig.1c. The magnitude parameter c and the time series $\phi(t)$ are the same to those in Sec.3.

a. Cross section of mean zonal velocity in the heating region

In order to assess the upscale impact of mesoscale fluctuations, two numerical simulations with either mesoscale zonally localized or uniform *deep2* heating are implemented for comparison. The difference of zonal velocity anomalies indicates the impact of eddy flux divergence of zonal momentum on the planetary-scale circulation. Fig.9a shows the cross section of planetary-scale zonal velocity anomalies in the center of the heating region at day 4 in the *deep2* heating case. The overall spatial pattern of zonal velocity anomalies here is quite similar to that in the planetary-scale zonal symmetric case in Fig.6c, including westerly wind anomalies in deep vertical extent near the latitude $y = 800$ km with its maximum strength in the middle troposphere and alternate mean zonal velocity anomalies in the middle troposphere near the equator. In contrast, Fig.9b shows the cross section of planetary-scale zonal velocity anomalies in the shallow heating case. Compared with the deep convective heating case in Fig.9a, the zonal velocity anomalies on the planetary scale are mostly confined in the lower troposphere, which is consistent with the limited vertical extent of the shallow congestus heating. Meanwhile, the spatial pattern of zonal velocity anomalies is quite similar to the planetary-scale zonally symmetric case in Fig.6f.

b. Mean zonal velocity in the lower, middle and upper tropospheres

The zonal velocity anomalies due to the eddy flux divergence of zonal momentum have different spatial patterns at different levels in Fig.9. Fig.10a-c shows planetary-scale zonal velocity anomalies at three different levels at day 4 in the *deep2* heating case. Firstly, the significant zonal velocity anomalies are confined in the longitudes between $X = 15 \times 10^3 km$ and $X = 25 \times 10^3 km$, which is the same as the zonal extent of the convective envelope in Eq.18. Secondly, the zonal velocity anomalies due to eddy flux divergence of zonal momentum have different spatial patterns at different levels. In the lower troposphere in Fig.10c, westerly wind anomalies are localized in the northern of the diabatic heating and weak easterly wind anomalies are to the south. In the middle troposphere in Fig.10b, the westerly wind anomalies at high latitudes of the Northern Hemisphere has stronger magnitude and broader zonal extent. Besides, there are easterly wind anomalies at low latitudes of the Northern Hemisphere and westerly wind anomalies to their south and north. Since the mean zonal winds in the middle troposphere near the equator are relatively weak, such significant zonal wind anomalies can dramatically change the zonal wind direction and magnitude. The zonal velocity anomalies in the upper troposphere in Fig.10a is dominated by westerly winds with broad meridional extent, including low latitudes of both the Northern and Southern Hemisphere as well as the equator. Such broad meridional extent of zonal velocity anomalies is related with the advection effects by the upper branch of the circulation cell in northerly returning flows. In contrast, planetary-scale zonal velocity anomalies at these three levels at day 4 in the shallow heating case are shown in Fig.10d-f. Similarly, the most significant planetary-scale zonal velocity anomalies are confined in the diabatic heating region between $X = 15 \times 10^3 km$ and $X = 25 \times 10^3 km$. At the surface in Fig.10f, there are westerly wind anomalies at high latitudes of the Northern Hemisphere and easterly wind anomalies to the south, whose spatial pattern is quite similar to the deep convective heating case in Fig.10c. In the middle troposphere in Fig.10e, easterly wind anomalies are found to the north of the westerly wind anomalies in the Northern Hemisphere, whose magnitudes are much weaker than those in lower levels. In the upper troposphere in Fig.10d, the magnitude of zonal velocity anomalies is negligible.

In the M-ITCZ equations, the planetary-scale physical variables including large-scale zonal velocity $\langle \bar{u} \rangle$, pressure perturbation Π, potential temperature anomalies Θ and secondary vertical motion W do not depend on meridional coordinate y, representing a planetary-scale gravity wave with uniform meridional profile. Therefore, the meridional mean of zonal velocity and potential temperature anomalies (not shown) can be used to characterize planetary-scale gravity waves. It turns out that the meridional mean of planetary-scale zonal velocity and potential temperature has few discrepancies with/without mesoscale fluctuations in both deep and shallow heating cases, meaning that little upscale impact of mesoscale fluctuations are transported away from the diabatic heating region by planetary-scale gravity waves.

5. Concluding Discussion

The ITCZ over the eastern Pacific is a narrow band of cloudiness, which is accompanied by low-level convergent winds and warm sea surface temperature below. Unlike the western Pacific ITCZ that migrates between the Northern and Southern Hemispheres in the seasonal cycle, the eastern Pacific ITCZ persistently remains in the Northern Hemisphere between the latitudes $5°N$ and $15°N$ throughout the whole year. Instead of being a steady state, the eastern Pacific ITCZ is sometimes observed to undulate and break down into several vortices, some of which become tropical cyclones and others dissipate and die out. As these tropical cyclones in great strength move to high latitudes, a new band of ITCZ cloudiness reforms in the original place. Capturing the flow fields in the baroclinic modes during the ITCZ breakdown including the undulation of a positive vorticity strip and the formation of a strong positive vortex is one of the main motivations in this paper. Using a multi-scale model to incorporate both the mesoscale and planetary-scale dynamics during the ITCZ breakdown and assessing the upscale impact of mesoscale fluctuations on the planetary-scale circulation is the other one of the main motivations.

Here a multi-scale model (M-ITCZ equations) is used to achieve those motivations as mentioned above. The M-ITCZ equations were first derived in (Biello and Majda 2013) by starting from the primitive equations on an equatorial β plane and following systematic multi-scale asymptotic methods (Majda and Klein 2003; Majda 2007). Two zonal spatial scales arise naturally from the physically scaling about atmospheric flow field in the ITCZ (mesoscale $L_m = 500$ km and planetary-scale $L_p = 5000$ km). The M-ITCZ equations describe atmospheric flows on both the planetary scale and mesoscale, and the corresponding governing equations across these two scales are nonlinearly coupled to each other. Specifically, the undulation of a positive vorticity strip and formation of a strong positive vortex are simulated on the mesoscale dynamics of the M-ITCZ equations, which resembles the formation of tropical cyclones during the ITCZ breakdown. The planetary-scale circulation is governed by the planetary-scale gravity wave equations in the M-ITCZ equations.

In the first scenario, the planetary-scale flow is assumed to be zonally symmetric, which suppresses planetary-scale gravity waves in the M-ITCZ equations. Such an idealized assumption isolates the upscale impact of mesoscale fluctuations from the planetary-scale gravity wave and provides a suitable scenario to model the ITCZ breakdown over several hundred kilometers in the mesoscale domain. Deep convective heating is prescribed as the mesoscale zonally localized heating in the Northern Hemisphere and uniform cooling elsewhere in the first baroclinic mode. First, after the flow field is initialized from a background state of rest, a positive vorticity strip forms at the surface in the northern side of the diabatic heating region, surrounded by negative vorticity anomalies. As the diabatic heating remains persistent, the positive vorticity strip has increasing magnitude and starts to undulate, which resembles the undulation of the ITCZ as observed in (Ferreira and Schubert 1997). Later, a strong positive vortex is generated in the middle of the positive vorticity strip, which mimicks tropical cyclogenesis in the baroclinic modes during the ITCZ breakdown. Since upward motion prevails in the diabatic heating region, positive vorticity anomalies are advected by upward motion and stretched vertically to the middle and upper troposphere. In the middle troposphere, a pair of vorticity dipoles are generated at low latitudes of the Northern Hemisphere, which also means cyclonic (anticyclonic) flows to the west (east) of the diabatic heating region. As the counterpart of the positive vorticity strip at the surface, negative vorticity anomalies with broad meridional extent are induced at the upper troposphere. Secondly, the eddy flux divergence of zonal momentum is characterized by mid-level (low-level) eastward (westward) momentum forcing with deep vertical extent at high latitudes of the Northern Hemisphere and mid-level alternate momentum forcing anomalies at low latitudes. Such eddy flux divergence of zonal momentum tends to induce westerly wind anomalies at high latitudes of the Northern Hemisphere, which are further advected by upper-level northerly winds to the Southern Hemisphere. Besides, mid-level easterly and westerly wind anomalies are also induced at low latitudes of the Northern Hemisphere, which provide extensive features for the zonal jets in this region. As far as the kinetic energy budget is concerned, acceleration effects are induced in the region where the positive vorticity anomalies are vertically stretched, while deceleration effects are mainly located in the lower troposphere to the north and south of the positive vorticity strip.

Besides, strong acceleration effects are also induced in the middle troposphere at low latitudes of the Northern Hemisphere, where the wind directions and strength are changed dramatically.

Compared with deep convective heating, shallow congestus heating is prescribed in a vertical profile with its maximum in the lower troposphere. After initialization from a background state of rest, a positive vorticity strip forms at the surface of the Northern Hemisphere, which undulates and generates a strong positive vortex in the middle. A direct comparison between the deep and shallow heating cases with the same maximum heating magnitude indicates that shallow congestus heating induces stronger vorticity anomalies and wind strength at the surface, which is related with the larger horizontal wind convergence there. In fact, such stronger cyclonic flows driven by shallow congestus heating is also discussed in a canonical balanced model to simulate "how towers" in the hurricane embryo (Majda et al. 2008). In the three-dimensional simulation for ITCZ breakdown of (Wang and Magnusdottir 2005) using a primitive equation model, shallow heating tends to induce stronger lower-tropospheric potential vorticity response than the deep heating while the upper-tropospheric potential vorticity response vanishes. Here, as upward motion prevails in the diabatic heating region, positive vorticity anomalies in the Northern Hemisphere is advected by upward motion and lifted up to the middle troposphere. The resulting large-scale circulation response is confined in the low and middle troposphere and vanishes in the upper troposphere, which resembles shallow meridional circulation as observed over the eastern Pacific. As far as the eddy flux divergence of zonal momentum is concerned, its spatial pattern in the shallow heating case is mostly confined in the lower and middle troposphere with eastward momentum forcing at high latitudes of the Northern Hemisphere and alternative eastward/westward momentum forcing anomalies at low latitudes. Shallow congestus heating also induces stronger eddy flux divergence of zonal momentum on the planetary-scale zonal winds. As for the kinetic energy budget, there are stronger acceleration effects in the region where the positive vorticity anomalies are vertically stretched and deceleration effects to its north and south. Besides, acceleration effects are also significant in the lower troposphere at low latitudes of the Northern Hemisphere.

In the second scenario, the two scales (planetary scale and mesoscale) are set to interact with each other and the diabatic heating is modulated by a planetary-scale zonally localized convective envelope to mimic the eastern Pacific ITCZ; The fully coupled M-ITCZ equations that allow zonal variation of flow fields on both the mesoscale and planetary scale are used. As studied in (Biello and Majda 2013), in the mean deep heating case, the resulting overturning circulation consist of the deep meridional circulation and zonal jets due to the Coriolis force. The meridional mean of planetary-scale zonal velocity is in the first baroclinic mode and propagates away with the planetary-scale gravity wave, which also brings negative (positive) potential temperature anomalies and upward (downward) motion to the west (east), providing favorable (unfavorable) conditions for convection. After replacing the mean heating by the mesoscale zonally localized heating, significant zonal velocity anomalies are induced in the diabatic heating region, which mainly consist of deep westerly wind anomalies at high latitudes of the Northern Hemisphere and several easterly/westerly wind anomalies in the middle troposphere near the equator. As modulated by the planetary-scale convective envelope, the flow fields in all the mesoscale domains are characterized by cyclonic flow in the same direction in the Northern Hemisphere. In the shallow heating case, most of significant zonal velocity anomalies induced by eddy flux divergence of zonal momentum are confined in the lower troposphere, although the spatial pattern in the corresponding levels are similar to that in the deep convective heating case. Lastly, the eddy flux divergence of zonal momentum has weak impact on the meridional mean of zonal velocity and potential temperature in both deep and shallow heating cases, thus small upscale impact of mesoscale fluctuations are transported away from the diabatic heating region by the planetary-scale gravity waves.

This study based on a multi-scale model has several implications for physical interpretation and comprehensive numerical models. First, the MEWTG equations in the idealized scenario with zonally symmetric planetary-scale flow successfully capture several key features of the ITCZ breakdown in the baroclinic modes, including the undulation of the positive vorticity strip and formation of a strong positive vortex. Secondly, the M-ITCZ equations model both the ITCZ breakdown and planetary-scale circulation in a self-consistent framework and provide assessment of the upscale impact of mesoscale fluctuations in a transparent fashion. Thirdly, compared with the deep convective heating, shallow congestus heating tends to have more significant upscale impact on the planetary-scale circulation including stronger eddy flux divergence of zonal momentum and acceleration/deceleration effects. Lastly, the resulting eddy flux divergence of zonal momentum significantly modifies planetary-scale zonal velocity, resulting in the rectification of the ITCZ over the eastern Pacific. Such assessment of the upscale impact of mesoscale fluctuations associated with the ITCZ breakdown can help to improve the convective parameterization in more complex numerical models. The M-ITCZ equations under the current model setup can also be generalized in several ways and used to model other phenomena in the ITCZ. For example, as suggested in (Biello and Majda 2013), instead of prescribing the diabatic heating, an active heating coupling the M-ITCZ equations with moisture will introduce new realistic features of tropical flows. As planetary-scale gravity waves propagate westward, negative potential temperature anomalies and upward motion are also carried westward, which provides favorable conditions for convection. The recently triggered convection through the active heating induces mesoscale fluctuations and generates upscale impact on the planetary-scale gravity wave in return. Such mesoscale Rossby wave coupled with planetary-scale gravity wave through an active heating can be a good candidate for westward moving disturbances as observed in the eastern Pacific ITCZ (Yang et al. 2003; Serra et al. 2008). In addition, coupling an equation for the atmospheric boundary layer can further elaborate the M-ITCZ equations and provide realistic features of tropical phenomena over the eastern Pacific. The resulting model should be useful to model the convective instability in the ITCZ and flow fields during the ITCZ breakdown.

Acknowledgments. This research of A.J.M is partially supported by the office of NAVAL Research ONR MURI N00014-12-1-0912, and Q.Y. is supported as a graduate research assistant on this grant. The research of B.K. is partly supported by a grant from the Natural Sciences and Engineering Research Council of Canada.

APPENDIX

Numerical Scheme

The M-ITCZ equations consist of two zonal spatial scales (planetary-scale and mesoscale), and the corresponding dynamics on these scales are coupled to each other in complete nonlinearity. A suitable numerical scheme is required to simulate this model without violating the following properties. First of all, the M-ITCZ equations are derived by using multi-scale asymptotic methods, which assume scale separation that these two zonal spatial scales are independent from each other when the small parameter (Rossby number ε) goes to zero in the asymptotic limit. Secondly, the MEWTG equations in Eqs.4a-4d are totally nonlinear with the advection term in three-dimensional flows. Thirdly, although both the mesoscale and planetary-scale dynamics are coupled with each other, a suitable averaging method need to be chosen so that large-scale physical variables can be obtained and updated in each time step. Lastly, the hydrostatic balance is valid on the planetary scale in Eq.1e, which requires a vertical boundary condition for the planetary-scale pressure perturbation. Such a numerical scheme shares many similar features with the so-called superparameterization method (Majda and Grooms 2014).

The numerical scheme for solving the M-ITCZ equations is split into two alternative steps. The first step is to solve the MEWTG equations in each mesoscale box and the second step is to solve the planetary-scale gravity wave equations in the full domain.

Step 1: solve the MEWTG equations in each single mesoscale box,

$$\frac{Du}{Dt} - yv = -\frac{\partial p}{\partial x} - du, \tag{A1a}$$

$$\frac{Dv}{Dt} + yu = -\frac{\partial p}{\partial y} - dv, \tag{A1b}$$

$$w = S_\theta, \tag{A1c}$$

$$\frac{\partial u}{\partial x} + \frac{\partial v}{\partial y} + \frac{\partial w}{\partial z} = 0, \tag{A1d}$$

and compute zonal and meridional averaging of u in each mesoscale box $\langle \bar{u} \rangle$.

Step 2: solve the planetary-scale gravity wave equations,

$$\frac{\partial \langle \bar{u} \rangle}{\partial t} + \frac{\partial \Pi}{\partial X} = 0, \tag{A2a}$$

$$\frac{\partial \Pi}{\partial x} = \frac{\partial \Pi}{\partial y} = 0,\ \frac{\partial \Pi}{\partial z} = \Theta, \tag{A2b}$$

$$\frac{\partial \Theta}{\partial t} + W = 0, \tag{A2c}$$

$$\frac{\partial}{\partial X}\left[\langle \bar{u} \rangle - U\right] + \frac{\partial W}{\partial z} = 0, \tag{A2d}$$

and update u in each mesoscale box by adding the increment of mean zonal velocity $\langle \bar{u} \rangle$.

a. Solve the MEWTG equations in each single mesoscale box

In order to solve the MEWTG equations, the Helmholtz decomposition is utilized to decompose horizontal velocity with stream function ψ and velocity potential ϕ,

$$u = -\frac{\partial \psi}{\partial y} + \frac{\partial \phi}{\partial x}, \tag{A3}$$

$$v = \frac{\partial \psi}{\partial x} + \frac{\partial \phi}{\partial y}, \tag{A4}$$

which turn out to be governed by two coupled Poisson's equations as follows ($\Delta = \frac{\partial^2}{\partial x^2} + \frac{\partial^2}{\partial y^2}$),

$$\Delta\phi = -\frac{\partial}{\partial z} S_\theta \tag{A5}$$

$$\Delta\psi = \xi \tag{A6}$$

$$\textit{BC1}\colon\ \phi, \psi \text{ are periodic in x}$$

$$\textit{BC2}\colon\ \frac{\partial\psi}{\partial x} + \frac{\partial\phi}{\partial y} = 0 \text{ at } y = \pm L_*$$

$$\textit{BC3}\colon\ -\frac{\partial\psi}{\partial y} + \frac{\partial\phi}{\partial x} = \bar{u} \text{ at } y = \pm L_*$$

Such technique is first used in the study (Majda et al. 2010, 2008). Here *BC1* denotes the local periodicity boundary condition in the zonal direction. *BC2* denotes rigid-lid condition for meridional velocity at the meridional boundaries. *BC3* assumes the mesoscale fluctuations of zonal velocity vanish in the meridional boundaries $u' = 0$, $u = \bar{u}$ and thus the governing equation for mean zonal velocity at the meridional boundaries can be derived by taking zonal averaging of Eq.A1a.

$$\frac{\partial\bar{u}}{\partial t} + \bar{w}\frac{\partial\bar{u}}{\partial z} = -d\bar{u}. \tag{A7}$$

Besides, the vorticity is governed by a forced advection equation in three-dimensional flows,

$$\frac{\partial\xi}{\partial t} + u\frac{\partial\xi}{\partial x} + v\frac{\partial\xi}{\partial y} + w\frac{\partial\xi}{\partial z} = (\xi + y)\frac{\partial S_\theta}{\partial z} - \frac{\partial v}{\partial z}\frac{\partial S_\theta}{\partial x} + \frac{\partial u}{\partial z}\frac{\partial S_\theta}{\partial y} - v - d\xi. \tag{A8}$$

which is solved by a second-order Corner-Transport-Upwind (CTU) scheme following (LeVeque 2002) with careful treatment of corner flux terms to maintain second-order accuracy in space. In addition, the predictor-corrector scheme is utilized to improve temporal accuracy with two stages. A cheap first-order upwind scheme is implemented in the first stage. After estimating the velocity field at half time step in the first stage, the second-order piecewise linear CTU scheme is applied to calculate the vorticity in the second stage.

b. Solve the planetary-scale gravity wave equations

It is well known that such linear equations in Eqs.A2a-A2d with rigid-lid boundary conditions can be solved with explicit solution formulas in both barotropic and baroclinic modes (Majda 2003). In particular, the harmonic functions (sine and cosine functions) are a complete set of basis functions, which also satisfy the rigid-lid boundary conditions in the vertical direction. Thus the linear planetary-scale gravity wave equations are solved through vertical mode decomposition with both the barotropic and baroclinic modes. Due to the zonally periodic boundary condition, the numerical scheme is further speeded up by using the Fast Fourier Transform technique.

Case 1, barotropic mode $q = 0$:

$$\frac{\partial U}{\partial t} + \frac{\partial \Pi_0}{\partial X} = 0, \tag{A9}$$

Here the barotropic mode of pressure perturbation Π_0 are assumed to be constant for simplicity.

Case 2, baroclinic modes $q > 0$

$$\frac{\partial U_q}{\partial t} + \frac{\partial \Pi_q}{\partial X} = 0, \tag{A10a}$$

$$\Pi_q = \Theta_q, \tag{A10b}$$

$$\frac{\partial \Theta_q}{\partial t} + W_q = 0, \tag{A10c}$$

$$\frac{\partial U_q}{\partial X} - q^2 W_q = 0. \tag{A10d}$$

References

Biello, J. A., and A. J. Majda, 2005: A new multiscale model for the madden-julian oscillation. *Journal of the atmospheric sciences*, **62 (6)**, 1694–1721.

Biello, J. A., and A. J. Majda, 2006: Modulating synoptic scale convective activity and boundary layer dissipation in the ipesd models of the madden–julian oscillation. *Dynamics of atmospheres and oceans*, **42 (1)**, 152–215.

Biello, J. A., and A. J. Majda, 2013: A multiscale model for the modulation and rectification of the itcz. *Journal of the Atmospheric Sciences*, **70 (4)**, 1053–1070.

Biello, J. A., A. J. Majda, and Coauthors, 2010: Intraseasonal multi-scale moist dynamics of the tropical atmosphere. *Communications in Mathematical Sciences*, **8 (2)**, 519–540.

Deser, C., 1993: Diagnosis of the surface momentum balance over the tropical pacific ocean. *Journal of climate*, **6 (1)**, 64–74.

Ferreira, R. N., and W. H. Schubert, 1997: Barotropic aspects of itcz breakdown. *Journal of the atmospheric sciences*, **54 (2)**, 261–285.

Gill, A., 1980: Some simple solutions for heat-induced tropical circulation. *Quarterly Journal of the Royal Meteorological Society*, **106 (449)**, 447–462.

Gray, W. M., 1979: Hurricanes: Their formation, structure and likely role in the tropical circulation. *Meteorology over the tropical oceans*, **77**, 155–218.

Gruber, A., 1972: Fluctuations in the position of the itcz in the atlantic and pacific oceans. *Journal of the Atmospheric Sciences*, **29 (1)**, 193–197.

Gu, G., and C. Zhang, 2002: Westward-propagating synoptic-scale disturbances and the itcz. *Journal of the atmospheric sciences*, **59 (6)**, 1062–1075.

Hack, J. J., W. H. Schubert, D. E. Stevens, and H.-C. Kuo, 1989: Response of the hadley circulation to convective forcing in the itcz. *Journal of the Atmospheric Sciences*, **46 (19)**, 2957–2973.

Hanson, K., A. F. Hasler, J. Kornfield, and V. E. Suomi, 1967: Photographic cloud climatology from essa iii and v computer produced mosaics. *Bulletin of the American Meteorological Society*, **48**, 878–883.

Houze, R. A., 2004: Mesoscale convective systems. *Reviews of Geophysics*, **42 (4)**.

Hubert, L., A. Krueger, and J. Winston, 1969: The double intertropical convergence zone-fact or fiction? *Journal of the Atmospheric Sciences*, **26 (4)**, 771–773.

Khouider, B., Y. Han, and J. A. Biello, 2012: Convective momentum transport in a simple multicloud model for organized convection. *Journal of the Atmospheric Sciences*, **69 (1)**, 281–302.

Khouider, B., and A. J. Majda, 2008: Multicloud models for organized tropical convection: Enhanced congestus heating. *Journal of the Atmospheric Sciences*, **65 (3)**, 895–914.

Kiladis, G. N., M. C. Wheeler, P. T. Haertel, K. H. Straub, and P. E. Roundy, 2009: Convectively coupled equatorial waves. *Reviews of Geophysics*, **47 (2)**.

LeVeque, R. J., 2002: *Finite volume methods for hyperbolic problems*, Vol. 31. Cambridge university press.

Lin, J.-L., 2007: The double-itcz problem in ipcc ar4 coupled gcms: Ocean-atmosphere feedback analysis. *Journal of Climate*, **20 (18)**, 4497–4525.

Lin, J.-L., M. Zhang, and B. Mapes, 2005: Zonal momentum budget of the madden-julian oscillation: The source and strength of equivalent linear damping. *Journal of the atmospheric sciences*, **62 (7)**, 2172–2188.

Majda, A., 2003: *Introduction to PDEs and Waves for the Atmosphere and Ocean*, Vol. 9. American Mathematical Soc.

Majda, A. J., 2007: New multiscale models and self-similarity in tropical convection. *Journal of the atmospheric sciences*, **64 (4)**, 1393–1404.

Majda, A. J., and J. A. Biello, 2004: A multiscale model for tropical intraseasonal oscillations. *Proceedings of the National Academy of Sciences of the United States of America*, **101 (14)**, 4736–4741.

Majda, A. J., and I. Grooms, 2014: New perspectives on superparameterization for geophysical turbulence. *Journal of Computational Physics*, **271**, 60–77.

Majda, A. J., and R. Klein, 2003: Systematic multiscale models for the tropics. *Journal of the Atmospheric Sciences*, **60 (2)**, 393–408.

Majda, A. J., M. Mohammadian, and Y. Xing, 2008: Vertically sheared horizontal flow with mass sources: a canonical balanced model. *Geophysical and Astrophysical Fluid Dynamics*, **102 (6)**, 543–591.

Majda, A. J., and S. N. Stechmann, 2008: Stochastic models for convective momentum transport. *Proceedings of the National Academy of Sciences*, **105 (46)**, 17 614–17 619.

Majda, A. J., and S. N. Stechmann, 2009: A simple dynamical model with features of convective momentum transport. *Journal of the Atmospheric Sciences*, **66 (2)**, 373–392.

Majda, A. J., Y. Xing, and M. Mohammadian, 2010: Moist multi-scale models for the hurricane embryo. *Journal of Fluid Mechanics*, **657**, 478–501.

Majda, A. J., and Q. Yang, 2016: A multiscale model for the intraseasonal impact of the diurnal cycle over the maritime continent on the madden–julian oscillation. *Journal of the Atmospheric Sciences*, **73 (2)**, 579–604.

Mapes, B. E., and R. A. Houze Jr, 1993: Cloud clusters and superclusters over the oceanic warm pool. *Monthly Weather Review*, **121 (5)**, 1398–1416.

Nolan, D. S., C. Zhang, and S.-h. Chen, 2007: Dynamics of the shallow meridional circulation around intertropical convergence zones. *Journal of the atmospheric sciences*, **64 (7)**, 2262–2285.

Philander, S., D. Gu, G. Lambert, T. Li, D. Halpern, N. Lau, and R. Pacanowski, 1996: Why the itcz is mostly north of the equator. *Journal of climate*, **9 (12)**, 2958–2972.

Ramage, C. S., 1968: Role of a tropical ”maritime continent” in the atmospheric circulation 1. *Monthly Weather Review*, **96 (6)**, 365–370.

Romps, D. M., 2014: Rayleigh damping in the free troposphere. *Journal of the Atmospheric Sciences*, **71 (2)**, 553–565.

Schneider, E. K., and R. S. Lindzen, 1977: Axially symmetric steady-state models of the basic state for instability and climate studies. part i. linearized calculations. *Journal of the Atmospheric Sciences*, **34 (2)**, 263–279.

Serra, Y. L., G. N. Kiladis, and M. F. Cronin, 2008: Horizontal and vertical structure of easterly waves in the pacific itcz. *Journal of the Atmospheric Sciences*, **65 (4)**, 1266–1284.

Sobel, A. H., J. Nilsson, and L. M. Polvani, 2001: The weak temperature gradient approximation and balanced tropical moisture waves*. *Journal of the atmospheric sciences*, **58 (23)**, 3650–3665.

Toma, V. E., and P. J. Webster, 2010a: Oscillations of the intertropical convergence zone and the genesis of easterly waves. part i: diagnostics and theory. *Climate dynamics*, **34 (4)**, 587–604.

Toma, V. E., and P. J. Webster, 2010b: Oscillations of the intertropical convergence zone and the genesis of easterly waves part ii: numerical verification. *Climate dynamics*, **34 (4)**, 605–613.

Waliser, D. E., and C. Gautier, 1993: A satellite-derived climatology of the itcz. *Journal of Climate*, **6 (11)**, 2162–2174.

Wang, C.-c., and G. Magnusdottir, 2005: Itcz breakdown in three-dimensional flows. *Journal of the atmospheric sciences*, **62 (5)**, 1497–1512.

Wang, C.-c., and G. Magnusdottir, 2006: The itcz in the central and eastern pacific on synoptic time scales. *Monthly weather review*, **134 (5)**, 1405–1421.

Winston, J. S., 1971: The annual course of zonal mean albedo as derived from essa 3 and 5 digitized picture data. *Mon. Wea. Rev*, **99 (11)**, 818–827.

Wu, Z., 2003: A shallow cisk, deep equilibrium mechanism for the interaction between large-scale convection and large-scale circulations in the tropics. *Journal of the Atmospheric Sciences*, **60 (2)**, 377–392.

Wyrtki, K., and G. Meyers, 1976: The trade wind field over the pacific ocean. *Journal of Applied Meteorology*, **15 (7)**, 698–704.

Yang, G.-Y., B. Hoskins, and J. Slingo, 2003: Convectively coupled equatorial waves: A new methodology for identifying wave structures in observational data. *Journal of the atmospheric sciences*, **60 (14)**, 1637–1654.

Yang, Q., and A. J. Majda, 2014: A multi-scale model for the intraseasonal impact of the diurnal cycle of tropical convection. *Theoretical and Computational Fluid Dynamics*, **28 (6)**, 605–633.

Zhang, C., 2001: Double itczs. *Journal of Geophysical Research*, **106 (D11)**, 11 785–11 792.

Zhang, C., 2005: Madden-julian oscillation. *Reviews of Geophysics*, **43 (2)**.

Zhang, C., M. McGauley, and N. A. Bond, 2004: Shallow meridional circulation in the tropical eastern pacific. *Journal of climate*, **17 (1)**, 133–139.

Zhang, C., D. S. Nolan, C. D. Thorncroft, and H. Nguyen, 2008: Shallow meridional circulations in the tropical atmosphere. *Journal of Climate*, **21 (14)**, 3453–3470.

LIST OF TABLES

Table 1. The multi-scale domain with nested grids and grid numbers and time steps in the numerical simulations. 55

Name	Symbol	Length of Domain	Grid Number	Resolution
planetary-scale zonal	X	$L_p = 4 \times 10^3 km$	41	$\Delta X = 0.976 \times 10^3 km$
mesoscale zonal	x	$L_m = 0.976 \times 10^3 km$	81	$\Delta x = 12.045 km$
meridional	y	$L_y = 3 \times 10^3 km$	241	$\Delta y = 12.5 km$
vertical	z	$L_z = 15.7 km$	127	$\Delta z = 0.125 km$
temporal	t	$T = 4 days$	1200	$\Delta t = 4.8 min$

TABLE 1. The multi-scale domain with nested grids and grid numbers and time steps in the numerical simulations.

LIST OF FIGURES

Fig. 1. Horizontal and vertical properties of heating profiles in all scenarios. (a) horizontal profile of zonally localized heating. (b) horizontal profile of zonally uniform heating. (c) vertical profiles of heating and its gradient. (d) time series of the vorticity at the surface in the Frobenius norm. The value is in dimensionless units. 58

Fig. 2. Horizontal profiles of velocity (arrow) and vorticity $\omega = v_x - u_y$ (color) in the longitude (horizontal axis, 10^3 km) and latitude (vertical axis, 10^3 km) diagram in the *deep2* heating case. The columns from left to right are for different heights from 0 km to 7.85 km to 15.7 km. The first three rows are for different days from Day 1 to Day 2 to Day 4. The last row is for the zonally uniform heating case. The panels in each column share the same color bar at the bottom. The maximum velocity magnitude is shown in the title of each panel and vorticity has units of day^{-1}. 59

Fig. 3. Horizontal profiles of velocity (arrow) and vorticity $\omega = v_x - u_y$ (color) in the longitude (horizontal axis, 10^3 km) and latitude (vertical axis, 10^3 km) diagram in the shallow heating case. The left column is for the height 0 km and the right column is for 7.85 km. The middle column is for *deep1* heating case at the height 0 km. The first three rows are for different days from Day 1 to Day 2 to Day 4. The panels in each column share the same color bar at the bottom. The maximum velocity magnitude is shown in the title of each panel and vorticity has units of day^{-1}. 60

Fig. 4. Vertical profiles of zonal velocity, meridional velocity and vorticity at Day 4. The columns from left to right are for zonal velocity, meridional velocity and vorticity. The first row (a-c) shows solutions along the latitude 0.8×10^3 km in the *deep2* heating case. The third row (g-i) shows solutions along the longitude 0.43×10^3 km in the *deep2* heating case. The second and fourth rows are the same as the first and third rows but for shallow heating case. The dimensional units of horizontal velocity and vorticity are ms^{-1} and day^{-1} respectively. . . 61

Fig. 5. Eddy flux divergence of zonal momentum F^U in the latitude-height diagram at day 4. The columns from left to the rights are for *deep2*, shallow and *deep1* heating cases. The second column share the same color bar at the bottom with the third column. The three panels from top to bottom are for (a) F^U, (b) its meridional component $-\frac{\partial}{\partial y}\left(\overline{v'u'}\right)$ (c) its vertical component $-\frac{\partial}{\partial z}\left(\overline{w'u'}\right)$. The dimensional unit of F^U is $ms^{-1}day^{-1}$. 62

Fig. 6. Mean zonal velocity $\bar{u}$ in the latitude-height diagram at day 4. The left panels from top to bottom show the solutions for (a) zonally localized heating, (b) zonally uniform heating, (c) their difference (a)-(b) in the *deep2* heating case. The right panels (d-f) show the same fields but for the shallow heating case. The dimensional unit of mean zonal velocity is ms^{-1}. . . . 63

Fig. 7. Acceleration and deceleration of mean zonal velocity due to eddy flux divergence of zonal momentum in the latitude-height diagram at day 4. The color indicates the value of the quantity $F^U\bar{u}$ with positive anomalies for acceleration effects and negative anomalies for deceleration effects. The panels from left to right are for the cases (a) *deep2*, (b) shallow, (c) *deep1*. The dimensional unit is $m^2s^{-2}day^{-1}$ 64

Fig. 8. A schematic depiction of the multi-scale domain with nested grids. The large red dots are the coarse grids on the planetary scale. Each coarse grid corresponds to a single mesoscale domain characterized by a mesoscale box in thick lines. The fine grids in each mesoscale domain are shown by pink dots. 65

Fig. 9. Cross section of mean zonal velocity anomalies in the center of heating region (longitude $X = 19.51 \times 10^3$ km) at day 4. The left panel is for *deep2* heating case and the right panel is for shallow heating case. The dimensional unit is ms^{-1}. 66

Fig. 10. Mean zonal velocity anomalies at different heights at day 4 in the longitude-latitude diagram. The left column (a-c) is for *deep2* heating case and the right column (d-f) is for shallow heating case. The panels from top to bottom are for heights 14.84 km, 7.48 km and 3.62 km respectively. The dimensional unit is ms^{-1}. 67

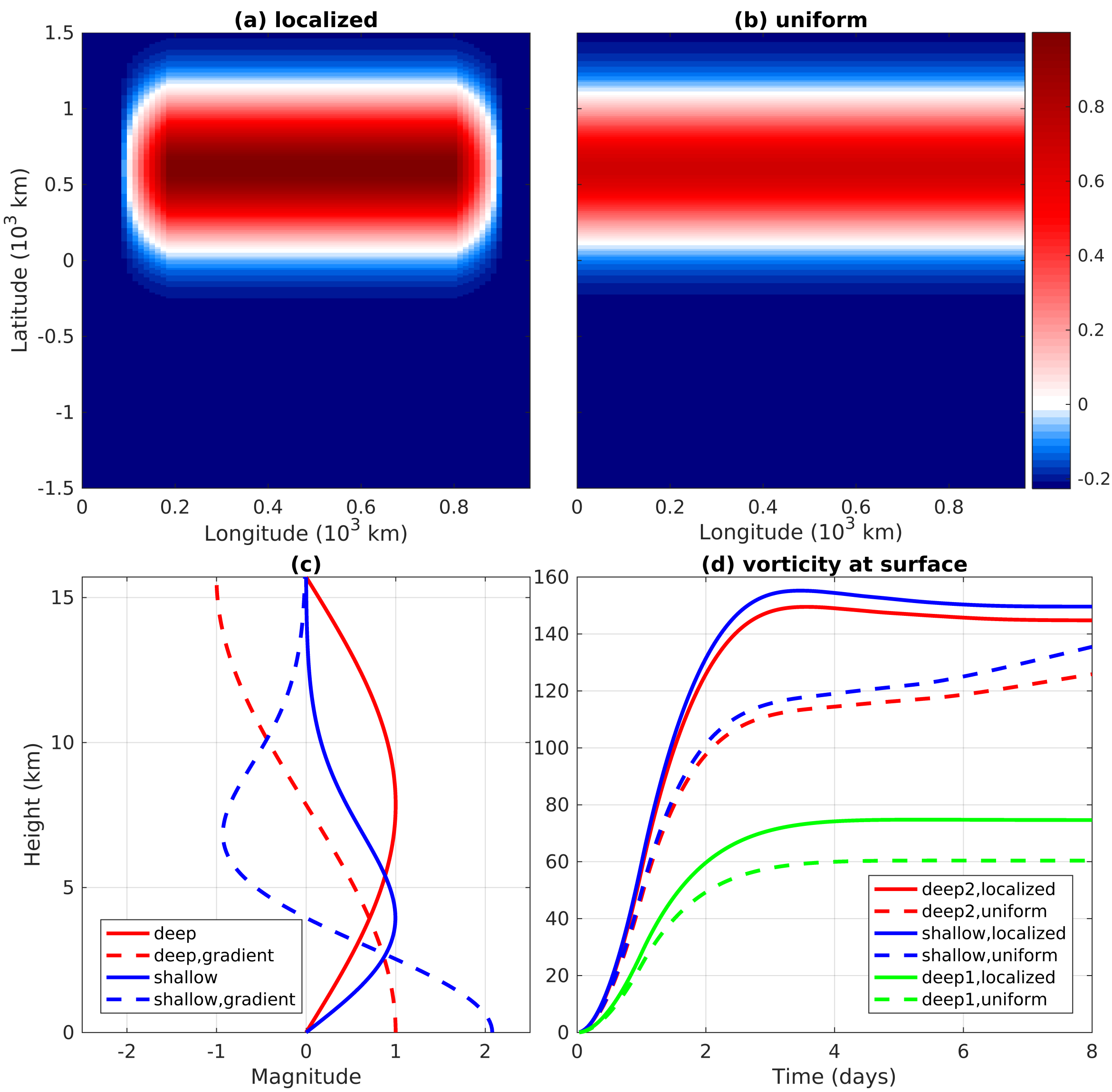

FIG. 1. Horizontal and vertical properties of heating profiles in all scenarios. (a) horizontal profile of zonally localized heating. (b) horizontal profile of zonally uniform heating. (c) vertical profiles of heating and its gradient. (d) time series of the vorticity at the surface in the Frobenius norm. The value is in dimensionless units.

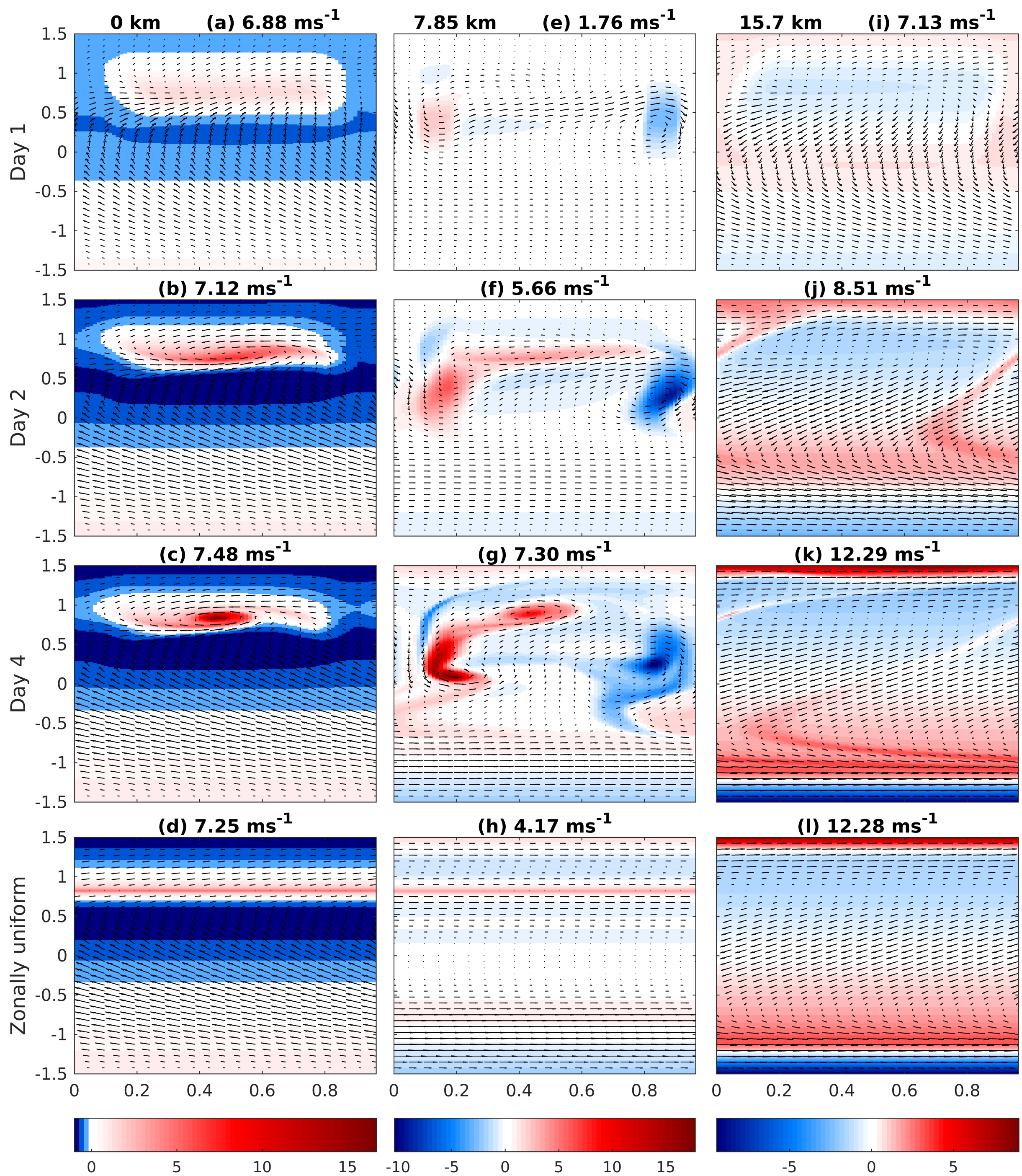

1157 FIG. 2. Horizontal profiles of velocity (arrow) and vorticity $\omega = v_x - u_y$ (color) in the longitude (horizontal axis, 10^3 km) and latitude (vertical axis, 10^3 km) diagram in the *deep2* heating case. The columns from left to right are for different heights from 0 km to 7.85 km to 15.7 km. The first three rows are for different days from Day 1 to Day 2 to Day 4. The last row is for the zonally uniform heating case. The panels in each column share the same color bar at the bottom. The maximum velocity magnitude is shown in the title of each panel and vorticity has units of day^{-1}.

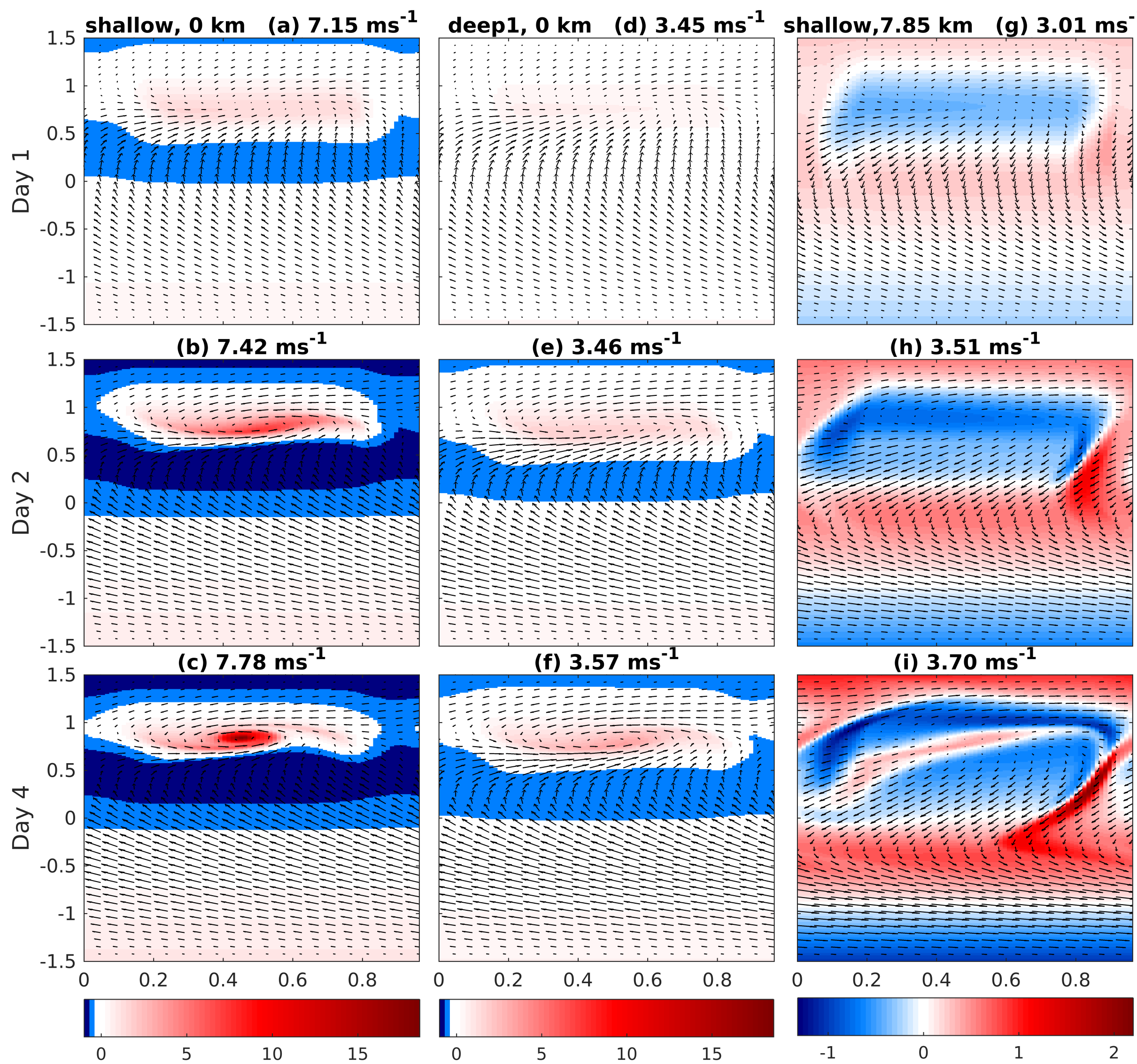

1163 FIG. 3. Horizontal profiles of velocity (arrow) and vorticity $\omega = v_x - u_y$ (color) in the longitude (horizontal axis, 10^3 km) and latitude (vertical axis, 10^3 km) diagram in the shallow heating case. The left column is for the height 0 km and the right column is for 7.85 km. The middle column is for *deep1* heating case at the height 0 km. The first three rows are for different days from Day 1 to Day 2 to Day 4. The panels in each column share the same color bar at the bottom. The maximum velocity magnitude is shown in the title of each panel and vorticity has units of day^{-1}.

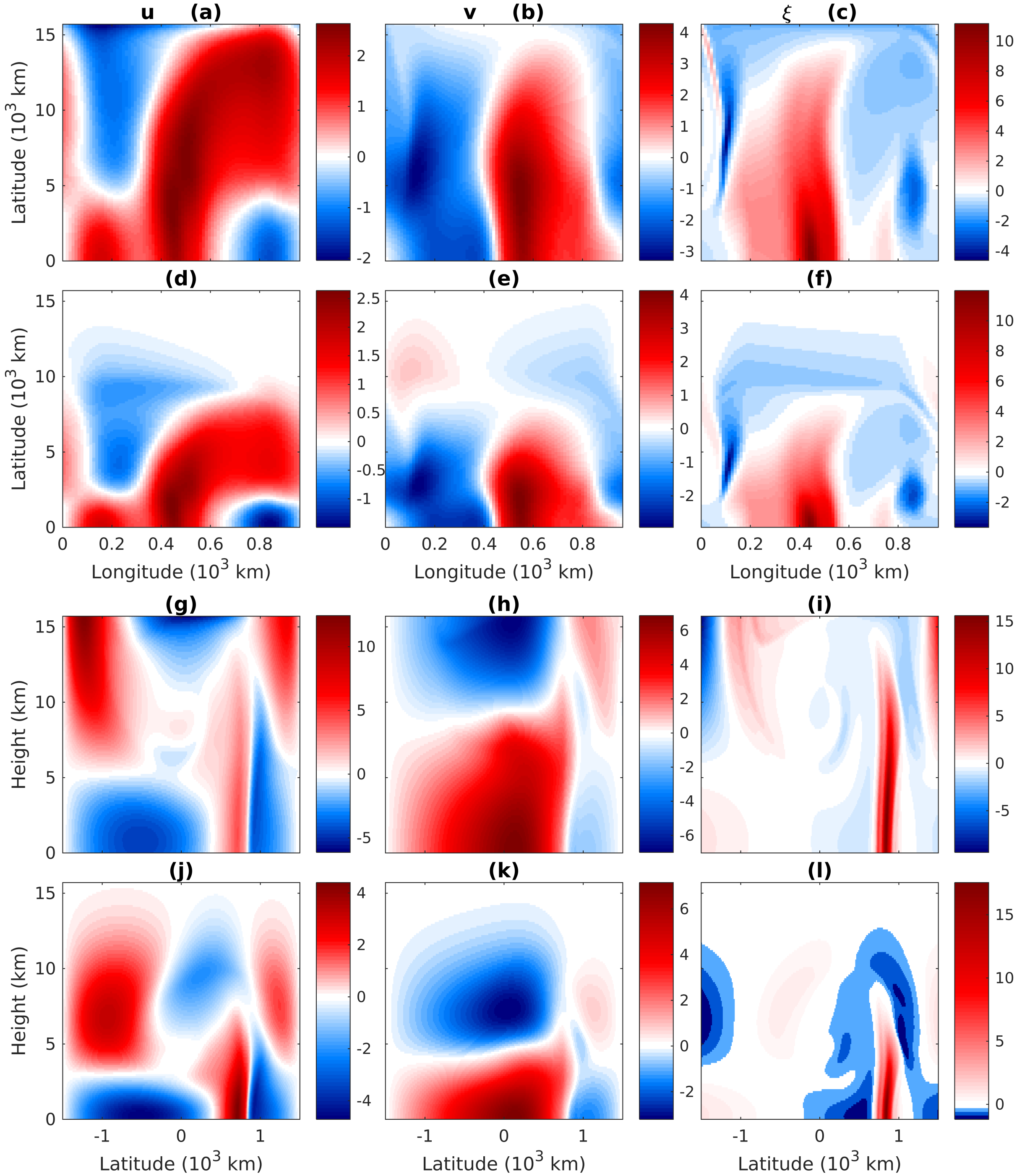

FIG. 4. Vertical profiles of zonal velocity, meridional velocity and vorticity at Day 4. The columns from left to right are for zonal velocity, meridional velocity and vorticity. The first row (a-c) shows solutions along the latitude 0.8×10^3 km in the *deep2* heating case. The third row (g-i) shows solutions along the longitude 0.43×10^3 km in the *deep2* heating case. The second and fourth rows are the same as the first and third rows but for shallow heating case. The dimensional units of horizontal velocity and vorticity are ms^{-1} and day^{-1} respectively.

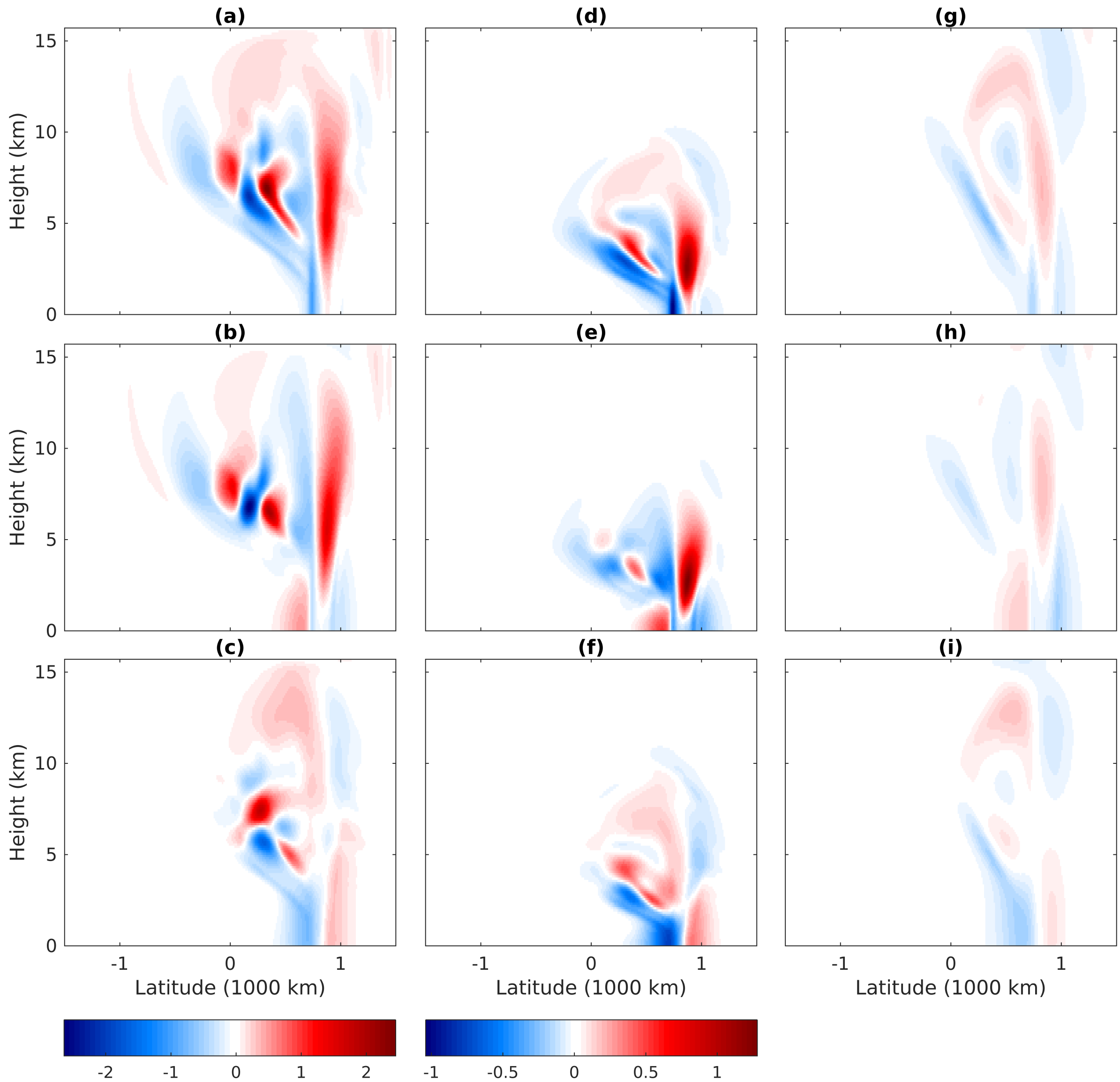

FIG. 5. Eddy flux divergence of zonal momentum F^U in the latitude-height diagram at day 4. The columns from left to the rights are for *deep2*, shallow and *deep1* heating cases. The second column share the same color bar at the bottom with the third column. The three panels from top to bottom are for (a) F^U, (b) its meridional component $-\frac{\partial}{\partial y}\left(\overline{v'u'}\right)$ (c) its vertical component $-\frac{\partial}{\partial z}\left(\overline{w'u'}\right)$. The dimensional unit of F^U is $ms^{-1}day^{-1}$.

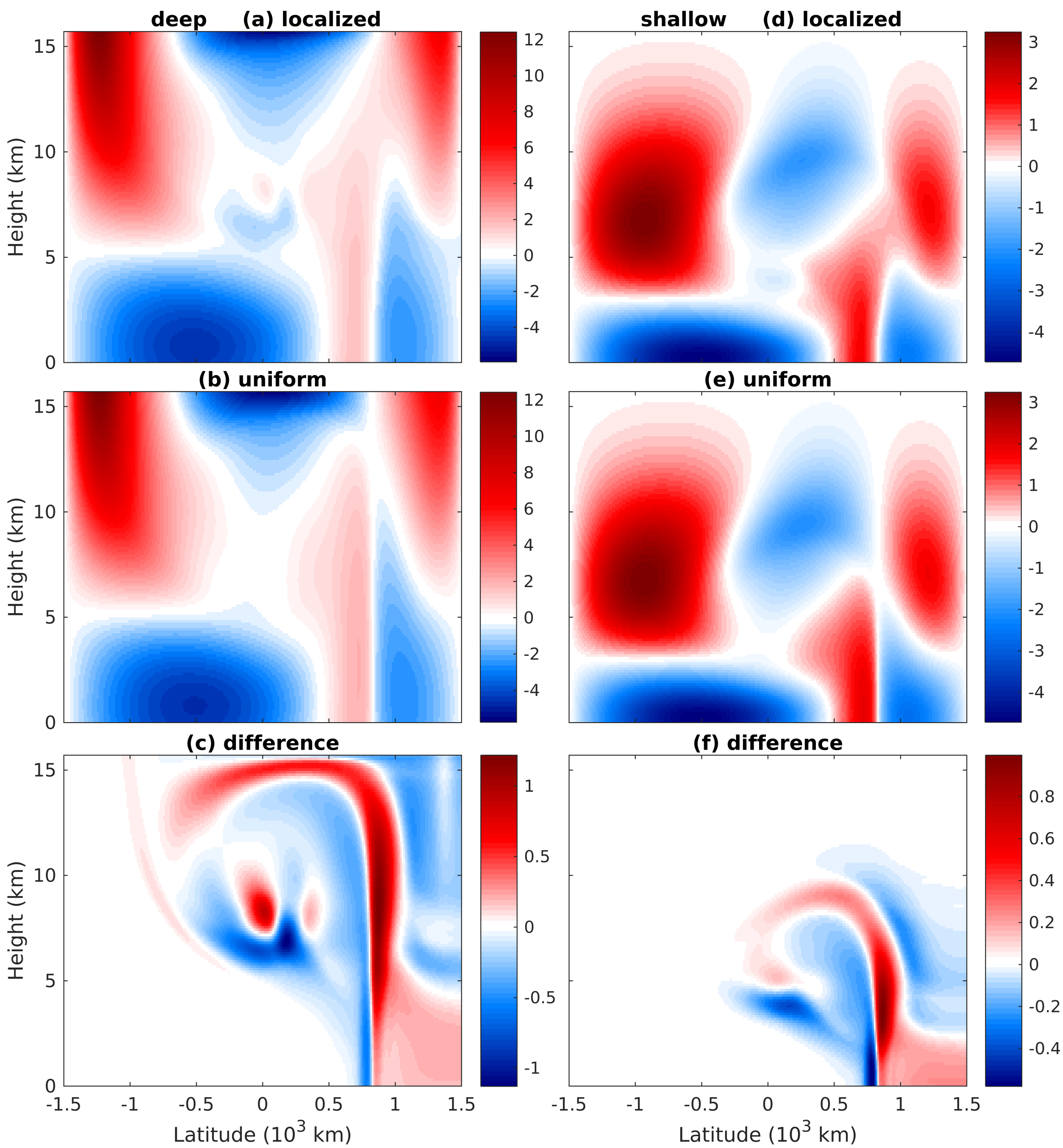

FIG. 6. Mean zonal velocity $\bar{u}$ in the latitude-height diagram at day 4. The left panels from top to bottom show the solutions for (a) zonally localized heating, (b) zonally uniform heating, (c) their difference (a)-(b) in the *deep2* heating case. The right panels (d-f) show the same fields but for the shallow heating case. The dimensional unit of mean zonal velocity is ms^{-1}.

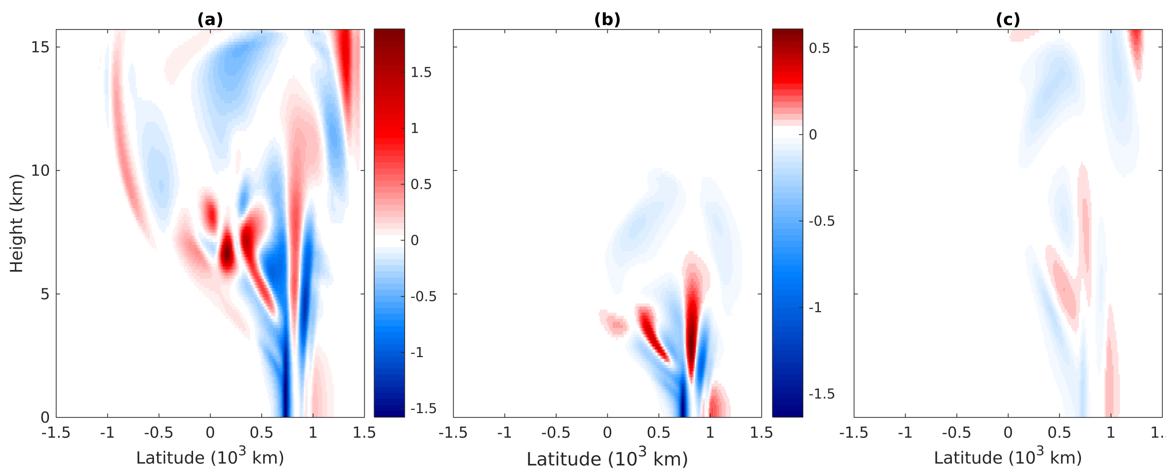

1183 FIG. 7. Acceleration and deceleration of mean zonal velocity due to eddy flux divergence of zonal momentum
1184 in the latitude-height diagram at day 4. The color indicates the value of the quantity $F^U \bar{u}$ with positive anomalies
1185 for acceleration effects and negative anomalies for deceleration effects. The panels from left to right are for the
1186 cases (a) *deep2*, (b) shallow, (c) *deep1*. The dimensional unit is $m^2 s^{-2} day^{-1}$

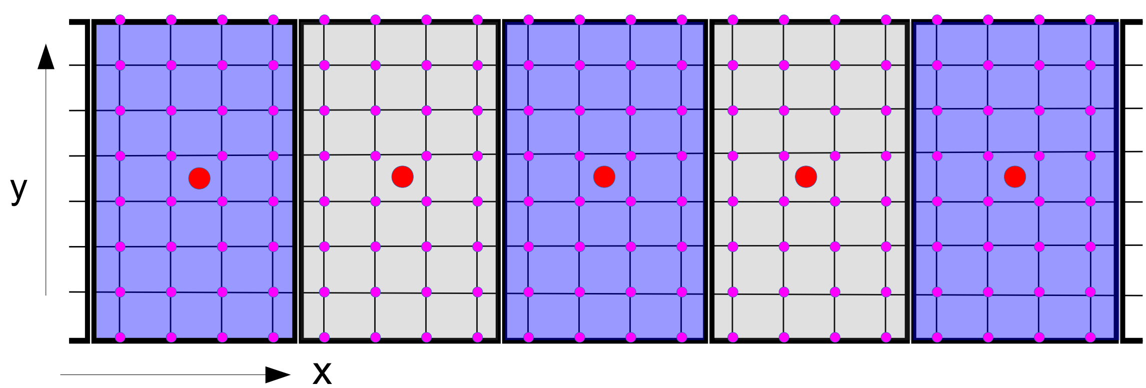

FIG. 8. A schematic depiction of the multi-scale domain with nested grids. The large red dots are the coarse grids on the planetary scale. Each coarse grid corresponds to a single mesoscale domain characterized by a mesoscale box in thick lines. The fine grids in each mesoscale domain are shown by pink dots.

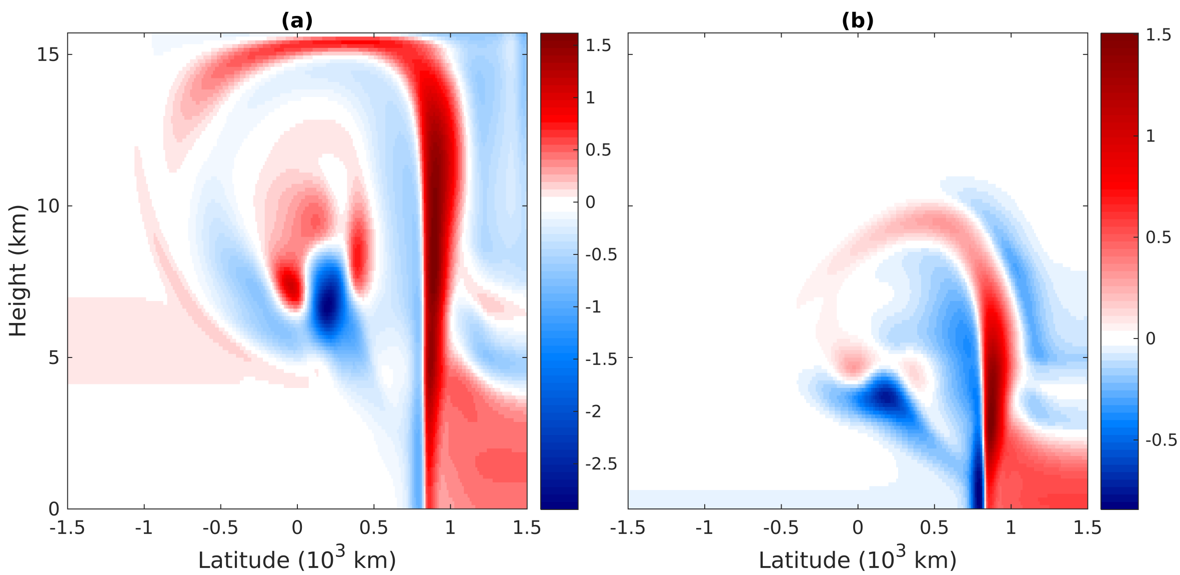

FIG. 9. Cross section of mean zonal velocity anomalies in the center of heating region (longitude $X = 19.51 \times 10^3$ km) at day 4. The left panel is for *deep2* heating case and the right panel is for shallow heating case. The dimensional unit is ms^{-1}.

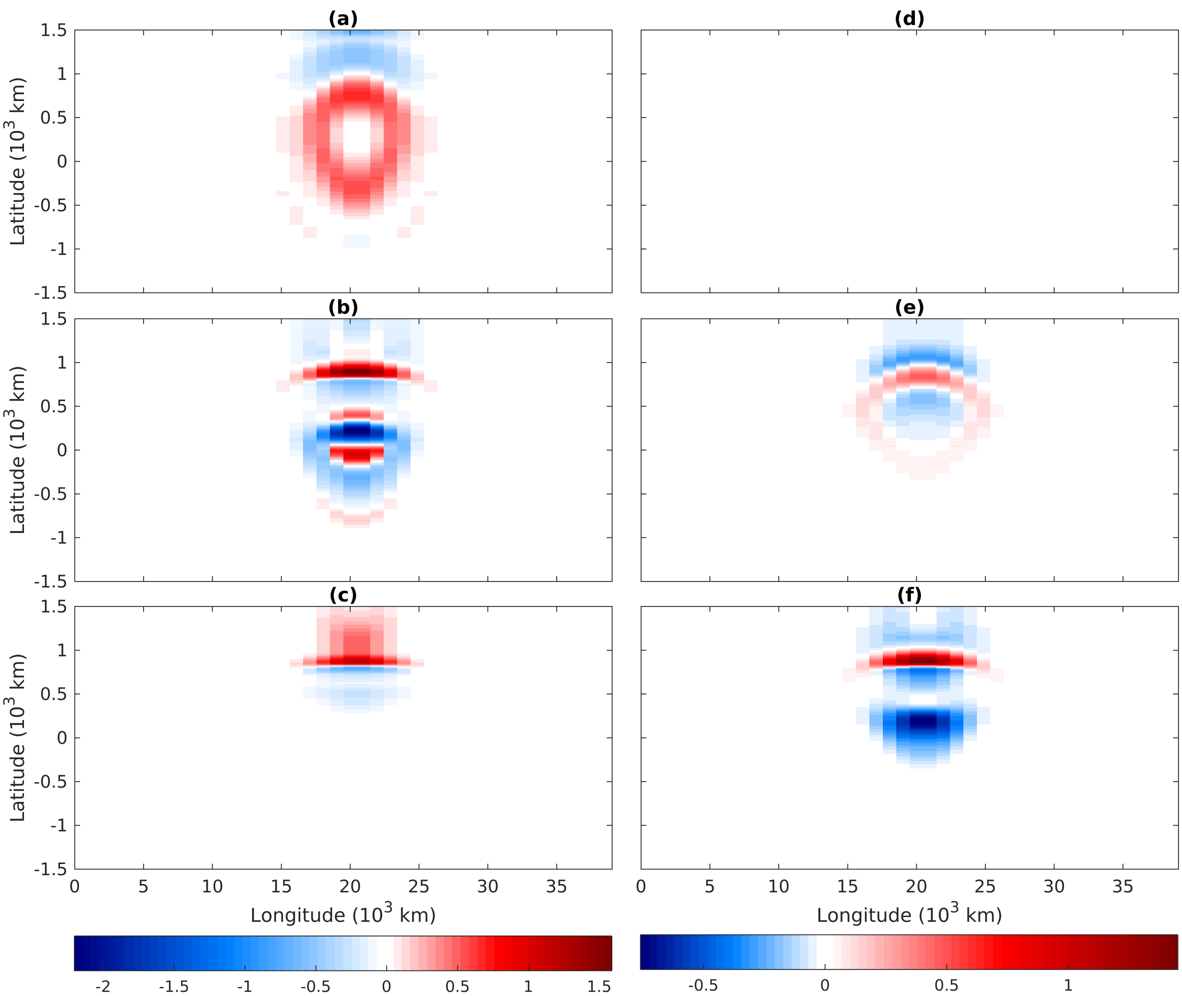

FIG. 10. Mean zonal velocity anomalies at different heights at day 4 in the longitude-latitude diagram. The left column (a-c) is for *deep2* heating case and the right column (d-f) is for shallow heating case. The panels from top to bottom are for heights 14.84 km, 7.48 km and 3.62 km respectively. The dimensional unit is ms^{-1}.